Boundary effects in Van der Waals materials

by

Daniel F. Hammerland

A thesis submitted to the

University of Colorado in partial fulfillment

of the requirements for the designation of

departmental honors

Department of Physics

2016

This thesis entitled:
Boundary effects in Van der Waals materials
written by Daniel F. Hammerland
has been approved for the Department of Physics

_____

Prof. Markus Raschke

_____

Prof. Paul Beale

_____

Prof. Adam Norris

Date _____

The final copy of this thesis has been examined by the signatories, and we find that both the content and the form meet acceptable presentation standards of scholarly work in the above mentioned discipline.

Hammerland, Daniel F. (Phyiscs)

Boundary effects in Van der Waals materials

Thesis directed by Prof. Markus Raschke

After the development of techniques for exfoliating [1, 2] and growing atomically thin crystals[3], transition metal dichalcogenides and graphene have both demonstrated having exceptional promise in applications of biosensing, spintronics, energy storage, and optoelectronics [4, 5, 6]. However, the electronic properties of these materials vary sensitively with crystal structure, orientation, number of layers, dopings and stacking order [7, 8, 9], making them highly sensitive to slight inhomogeneities. In order to optimally implement them for technological applications, we must first understand how these structural variations affect the material properties. Additionally, the small scale of these defects, on the order of a few nanometers, makes traditional spectroscopic analysis of these features difficult, impeding our ability to further our knowledge of them and ultimately limiting our ability to implement them in technology. In the last two decades, methods have been developed for overcoming these limitations [10]. Of these, Atomic Force Microscopy (AFM) and scattering-type Scanning Near-Field Optical Microscopy (s-SNOM) have been shown to be powerful tools for observing light-matter interactions at sub-diffraction length scales and imaging with spatial resolution at the deep sub-wavelength scale [11]. In this thesis, I implement AFM, s-SNOM, and Raman spectroscopy in order to identify stacking layer grain boundaries in graphene as well as to study the nanoscale properties of two phases of $MoTe_2$ and to investigate an optically induced phase transition in MoTe2.

Dedication

vavwI' chongaghpa' Dunmo' ngIl 'ej vIjaHnIS reH tu'lu'.

To my father for daring me to do better and to my mother for always being there.

Acknowledgements

I would like to thank everybody who has helped in my personal development as an individual and a scientist. Particularly, I would thank Joanna Atkin, Omar Khatib, Brian O'Callahan, Eric Muller, Sam Berweger, Vasily Kravtsov, and Ben Pollard for their infinite patience, excellent explanations, and guidance in my development as a scientist. I would like to especially thank Markus Raschke for giving me the opportunity to be so deeply involved at the forefront of an exciting field. I'd also like the specifically thank my parents for allowing me to attend school and supporting me through every step of it. Without the help, encouragement and inspiration of all of you I could never have made it this far. Thank you!

Contents

Chapter

Figures

Figure

Chapter 1

Introduction

1.1 Motivation

New materials have always been at the forefront of new technologies. The last century has seen incredible scientific progress in our ability to study and understand and control the properties of substances. The cutting edge of material science now focuses on nanoscale.

The last decade in particular has seen the discovery of a broad number of atomically thin, two dimensional materials[4, 5, 6]. These have promise in many technological applications such as optoelectronics, spintronics, biosensing, and energy storage[4, 5, 6] as well as providing an environment for novel physics due to their unique spatial confinement and symmetry[11]. Due to the high degree of symmetry and spatial confinement, slight alterations in these systems such as lattice mismatches and impurities can have drastic effects. Additionally, current techniques for fabricating these materials have not yet developed methods of minimizing and controlling these defects[1, 2, 3] . In order to further our knowledge of the underlying physics behind these materials and ultimately implement them in technology, we must have a strong understanding of how these defects affect electronic, optical, and structural properties in order to work around them or utilize them for our benefit.

Numerous methods exist for studying these effects directly with electrons, such as scanning tunneling microscopy (STM) and scanning electron microscopy (SEM) [12]. However, even these techniquess do not give a full picture. To complement these methods, insight from light matter interactions is invaluable. Reckoning the small length scales of these materials and light becomes

problematic due to the diffraction limit, an inherent quality of light arising from its wave nature. This limit inhibits our ability to use light of certain energy to understand properties on length scales less than a fraction of the incident wavelength of light being used. This, in turn, limits our ability to understand nanoscale defects and properties, especially at energies corresponding to large wavelengths[11].

Fortunately, the last several decades have seen the development of several methods of surpassing this limit[10, 11]. Nanoscale imaging techniques such as atomic force microscopy (AFM) and near-field optical techniques such as scattering scanning near-field optical microscopy (s-SNOM) have proven of particular use for probing the nanoscale properties of these materials. In atomic force microscopy (AFM), these tips are brought into contact with or are held within several nanometers of the sample, interacting with the physical features of the sample to acquire nanoscale images of the topography of the sample. In s-SNOM, light is additionally focused on to the AFM tip. This leads to nonpropgating solutions to Maxwell's equations emanating from the apex of the tip [11]. These fields are not limited by the diffraction limit and are known as evanescent waves. Conveniently, the tip also acts as a local scatterer, leading to Rayleigh scattering, which converts the evanescent field signal into a propagating field that can be measured in the far-field. Using these method, we can measure optical fields at resolution up to 1000x greater than is capable with far-field techniques[13]. Using this methods, we can explore the heterogeneities of 2D materials, gaining new physical insight and furthering our understanding of these technologically promising materials.

1.2 Overview

In this thesis, I investigate how the nanoscale structure of few layer graphene and $MoTe_2$ affect their optical properties. I study these materials through the implementation of Raman scattering, tapping mode atomic force microscopy, and phase resolved s-SNOM. Raman microscopy has proven invaluable to assess of 2D materials thickness[11] and can be used to study structural properties such as chemical interactions, lattice structure, phonon modes, and composition. Atomic force

microscopy allows us to detect the profile of samples on levels far bellow what is allowed by visible light, allowing us to resolve the nanoscopic dimensions of substances. s-SNOM takes an AFM and adds the ability to probe light matter interactions on similar scales. This tool allows us to investigate how nanoscale features can affect carrier densities and other electronic properties by capturing effects that cannot be seen in the physical topography such as grain boundaries and lattice junctions[8].

In particular, I examine the use of s-SNOM in order to identify stacking order defects in lattices of bilayer graphene. These boundaries are of high interest for the fabrication of microscopic electronic devices as they have increased carrier densities[8]. I also investigate a recently reported optically induced phase transition in $MoTe_2$[14]. In this transition a semiconducting state, the 2H phase of $MoTe_2$, is altered into the conducting 1T' phase by focusing a laser onto the structure. I induce and probe this transition with the use of Raman spectroscopy and then investigate the nanoscale optical properties of the final and initial states in the IR with the use of s-SNOM. These materials have not been well documented in the near-field, so I also investigate the general properties of the unaltered phases. I finish by discussing how these data compare with near-field microwave measurements performed by a collaborator, Samuel Berweger, at the National Institute of Standards and Technology (NIST).

1.3 Far-field optics

Traditional spectroscopy and microscopy utilize wave-like electromagnetic fields (light) and various lensing techniques in order to resolve microscopic features and to obtain information about their optical properties on the length scale of the wavelength of the light or larger. Commonly, either methods uses an objective or lens to focus light onto the sample. In microscopy, where the goal is to resolve the surface of the sample, the light is scattered off features and collimated for observation. In spectroscopy, the primary goal is not to resolve a space, but to see how the light of specific energies interacts with the sample. The scattering process is similar, but the emitted light is sent to a spectrometer to determine how the wavelengths of light being used and the energy

Figure 1.1: Images of a a) schematic for the variables associated with the diffraction limit and b) the "airy disc" of the diffraction limit, created by moving two points a distance below the diffraction limit. Notice that the two shapes are overlapping, prohibiting observation of them both simultaneously. Image credit to [11].

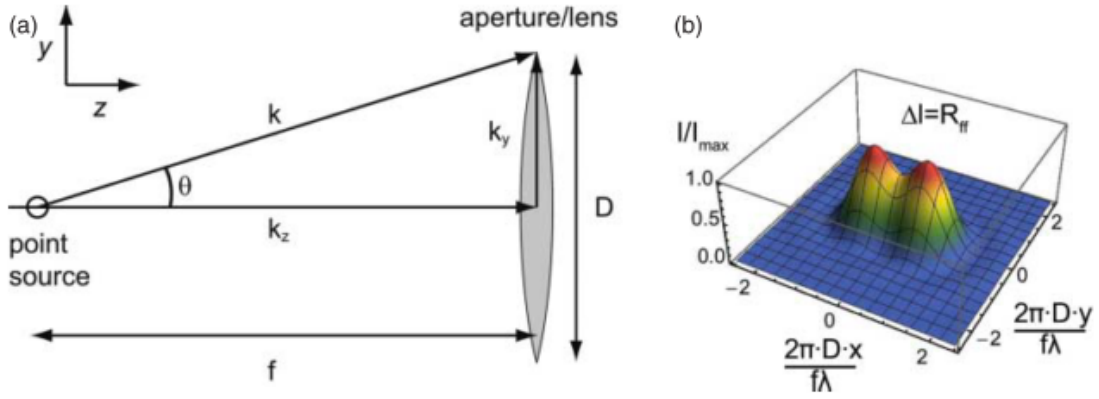

states of the material interact. Because both techniques utilize light that is scattered off objects, the resolution of these systems is then limited as the two objects become indistinguishable as they move closer together as demonstrated in Figure 1.1. This effect is described by Abbe's law[11],

$$D_{limit} = \frac{\lambda}{n * \sin(\theta)}, \tag{1.1}$$

where D_{limit} is the smallest resolvable scale, λ is the wavelength, n is the refractive index, and θ is the focusing angle, these can be seen in Figure 1.1a. This relationship inhibits our ability to resolve features or perform spectroscopy at any distance smaller than a fraction of the incident wavelength. Initial attempts to resolve nanoscale objects attempted to cope with the diffraction limit. This can be done in several basic ways. One method is to increase the numerical aperture, $n\sin(\theta)$, of the system. This can be done by either acquiring a tighter focus, increasing the $\sin(\theta)$ term in Equation 1.1, or by switching to medium with a larger index of refraction, increasing n in Equation 1.1. However, both of these methods have practical limits and, ultimately, the practical combination of these methods together allows an increase in resolution of less than an order of magnitude[15].

Smaller resolutions can be achieved with shorter wavelengths, through the use of x-rays and electrons. This is the concept behind methods such as scanning electron microscopy (SEM) and transmission electron microscopy(TEM)[12]. These techniques often are destructive to samples and require strict sample preparation that is not possible for all materials, making these methods impractical in many situations. Additionally, these methods do not give us a full spectroscopic understanding of the materials, leaving a substantial gap in our knowledge. However, the development of scanning probe microscopy (SPM) and subsequently of near-field optics introduced a method of nanoscale imaging and light matter interactions that rely on near-field interactions, and thus are not limited by the diffraction limit[13]. These techniques have proven invaluable in assessing the heterogeneities of modern nanomaterials.

Chapter 2

Background and theory

2.1 Two dimensional (2D) materials

The last decade has seen incredible progress in the fabrication and application of novel materials. Their atomically thin structures, unique symmetry and spatial confinement lead to unique physical properties that cannot exist in bulk materials. These materials are atomically thin and the varying layers interact solely through Van der Waals forces. This allows them to be mechanically exfoliated [1, 2] into atomically thin samples. Alternatively, they can be grown with chemical vapor deposition(CVD) [3]. Mechanical exfoliation provides samples with fewer defects than CVD, yet is less reproducible and does not usually create large samples [3]. While these samples are still quite small, a few hundred microns at the largest [2], they have speculated applications in a wide variety of fields varying from aerospace [16] to optoelectronics and energy storage [17].

Current interest focus mainly on novel nano-electronic devices. 2D materials have been shown to have great promise on their own [18, 19, 5], however, their true potential exist in heterostructures of these materials. In these devices, material lattices are alternated between in order to fine tune the properties of the materials. This can be difficult in traditional bulk electronics as mismatches can occur in the chemical bonds between the lattices, as seen in Figure 2.1a. However, in 2D materials, the adjacent layers interact solely via Van der Waals forces. Additionally, this allows for the easy stacking of different materials on top of each other. These systems would be highly tunable to a wide variety of applications in technology [20]

The large number of these materials that are being discovered adds further value to these

Figure 2.1: a) Mismatches in the lattices prevents proper bonding between different structures, inhibiting the abilities of bulk heterostructures in contrast to 2D materials, b) which can be stacked without dislocations because the sheets interact weakly. Image credits to [21]

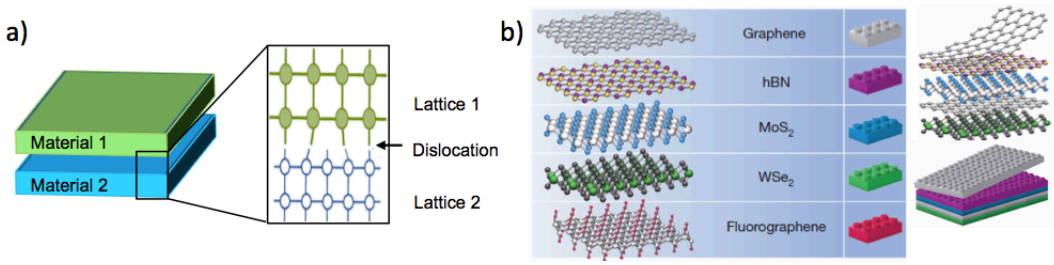

materials applications in technology. Several of them exist in unique phases that can vary drastically in their properties, such as $MoTe_2$, which can exist both as a conducting state and a semiconducting state based upon the strain exhibited on the lattice [22]. Overall, these material have demonstrated their ability to revolutionize electronics[4, 20].

However, before we can fully implement these materials, we must first better understand their nanoscale properties. They often suffer from defects in their lattices that can drastically alter their behavior, acting as dopants and often disrupting the symmetry of the system [18, 17, 8]. All of these properties must be understood before we can optimally implement them.

2.1.1 Graphene

Graphene was the first 2D material to be isolated and studied[19]. It is a hexagonal lattice of carbon atoms bonded by hybridized sp^2 orbitals [11]. In it monolayer form, it has a band structure with a linear energy-momentum relationship near the Dirac point, which ultimately makes it a zero gap semiconductor [11]. Bilayer structures of graphene have a tunable band gap that can be varied by applying an external electric field applied perpendicular to the surface. [8]. Additionally, it can contain stacking order differences based on the relative alignment of atoms between different layers. These orders can change, leading to a long boundary, which have been shown to be an ideal

candidate for explore valleytroncis and other forms of topological transport [8].

2.1.2 Transition metal dichalcogenides (TMDCs)

Even among the ever-growing list of 2D materials, transition metal dichalcogenides(TMDCs) have received large amounts of attention. These materials have a composition of the form MX_2, where M is a transition metal (Mo, W) and X is a chalcogen (S, Se, Te). These crystalline materials form in layers that are 3 atoms thick, which are then are subsequently stacked on top of each other. TMDC's have varying properties depending on how many layers are present [20]. Monolayer structures of many of these materials exhibit a direct band gap [23]. A direct band gap means that in a plot of energy momentum space, the valence band maximum and conduction band minimum lay on the same vertical line, corresponding to both states having identical momenta. Thus electrons can be excited from the valence band to the conduction band without any transfer of momentum. Therefore, these transitions can occur solely by photo-excitation without mediation by phonons. The ability to excite these systems optically makes them highly efficient and a prime candidate for spintronics and optoelectronics [4, 5, 6].

Figure 2.2: Two different lattice structures for transition metal dichalcogenides. We can see that the 2H phase is hexagonal relative to the distorted octahedral 1T' phase. Image credit to [20]

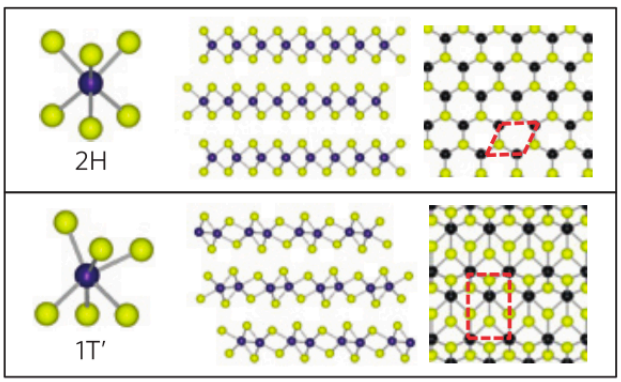

2.2 Properties of metals and doped semiconductors

2.2.1 plasma frequency

Both metals and semiconductors are characterized by free electrons in a fixed lattice and an overall net zero charge. Due to this fact, these materials can be modeled as plasmas [24]. The Drude-Lorentz model predicts the relative permeability of a metal when driven by an external oscillating electric field. The electrons exhibit no linear restoring force and are damped. This leaves us with the initial differential equation,

$$m_0 \frac{d^2x}{dt^2} + m_0\gamma \frac{dx}{dt} = -eE_0 e^{-i\omega t}, \tag{2.1}$$

where m_0 is the mass of an electron, x is the electron's position, γ is the damping, e is the charge of an electron, E is the magnitude of the applied electric field, and ω is the frequency of the electric field. To aid in finding a solution, we perform a change of variables to an oscillating position,

$$x = x_0 e^{-i\omega t}.$$

Evaluating the derivatives and substituting into Equation 2.1 we find,

$$-m_0\omega^2 x_0 e^{-i\omega t} - im_0\omega\gamma x_0 e^{-i\omega t} = -eE_0 e^{-i\omega t}.$$

Canceling the exponential and rearranging to find x_0,

$$x_0 = \frac{eE_0}{m_0(\omega^2 + i\gamma\omega)}. \tag{2.2}$$

The polarization of the electron gas, P, and the displacement field, D, are defined respectively,

$$P = -NE_0 x, \tag{2.3}$$

$$D = \epsilon_r\epsilon_0 E = \epsilon_0 E + P, \tag{2.4}$$

where N is the number of electrons per unit volume, ϵ_0 is the permittivity of free space, and ϵ_r is the permittivity of the sample. Now, we substitute x_0 into P, and P into D resulting in,

$$D = \epsilon_0 E - \frac{N e^2 E}{m_0(\omega^2 + i\omega\gamma)}. \tag{2.5}$$

From this, can extract a formula for ϵ_r by dividing by ϵ_0 and E,

$$\epsilon_r = 1 - \frac{N e^2}{\epsilon_0 m_0} \frac{1}{\omega^2 + i\omega\gamma}, \tag{2.6}$$

The coefficient on the second term of this series is the square of the plasma frequency, ω_p,

$$\omega_p = \left(\frac{N e^2}{\epsilon_0 m_0}\right)^{\frac{1}{2}}. \tag{2.7}$$

As an aside, the equation above can be generalized to doped semiconductors as well by substituting m^* for m_0, which is the effective mass of the electron in the system, and ϵ_0 for ϵ_{opt}, which is the square of the index of refraction of the undoped semiconductor. This leaves us with,

$$\omega_p = \left(\frac{N e^2}{\epsilon_{opt} m^*}\right)^{\frac{1}{2}}. \tag{2.8}$$

Returning to the case for metals, if we assume that the damping is small (a fair approximation as the resistance in metals is usually quite low) we can then reduce ϵ_r to,

$$\epsilon_r = 1 - \frac{\omega_p^2}{\omega^2}. \tag{2.9}$$

The complex index of refraction, $\tilde{n}$ is related to ϵ_r by,

$$\tilde{n} = \epsilon_r^{\frac{1}{2}}. \tag{2.10}$$

Further, the reflectance, R, of the metal is related to $\tilde{n}$ according to,

$$R = \|\frac{\tilde{n} - 1}{\tilde{n} + 1}\|^2. \tag{2.11}$$

Figure 2.3 shows the reflectance of a metal, with a $\omega_p = 1$, as a function of the frequency. We find that the reflectance has a value of 1 until once reaches ω_p, at which point it drops to zero. The plasma frequency, ω_p, is the maximum frequency that electrons can oscillate in the metal to cancel out the incident field. At frequencies lower than this, their oscillations screen the field and make the surface completely reflective; above this threshold the metal appears to be "transparent" [24].

Figure 2.3: Plot of the non-dimensionalised reflectance.

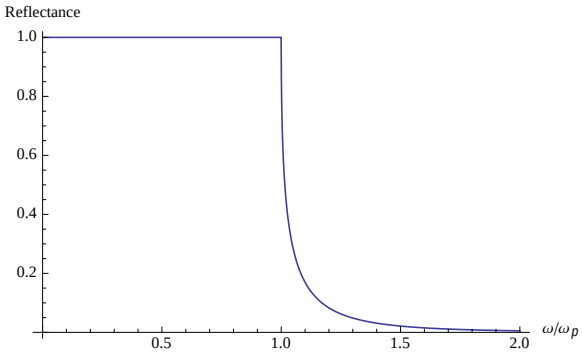

2.2.2 Plasmons

We have thought of metals and doped semiconductors as plasmas consisting of electrons in a positive nuclear lattice. These electrons flow freely, so the charge densities in these areas can fluctuate, creating a local high density of charge that is then repelled by the Coulomb force. The energy gained in the repulsion then displaces them past their original position, creating a form of oscillation [24]. This can be explained mathematically by beginning with Maxwell's equations and the charge continuity equation,

$$\bigtriangledown \cdot \mathbf{J} = \frac{-\partial \rho_e}{\partial t}, \tag{2.12}$$

where $\mathbf{J}$ is the current density, and ρ_e is the charge density of electrons. We can substitute ρ_e from Gauss's law to get,

$$\bigtriangledown \cdot \left(\mathbf{J} + \epsilon_0 \frac{\partial \mathbf{E}}{\partial t} \right) = 0,$$

where ϵ_0 is the permittivity of free space. The term in parentheses can be recognized as the Maxwell Ampere equation multiplied by ϵ_0.

$$\mathbf{J} + \epsilon_0 \frac{\partial \mathbf{E}}{\partial t} = \frac{1}{\mu_0} \bigtriangledown \times \mathbf{B}.$$

We can then proceed by taking a time derivative of both sides giving,

$$\frac{\partial \mathbf{J}}{\partial t} + \epsilon_0 \frac{\partial^2 \mathbf{E}}{\partial t^2} = \frac{1}{\mu_0} \bigtriangledown \times \frac{\partial \mathbf{B}}{\partial t}.$$

Plugging in the Maxwell-Faraday law for the right side gives,

$$\frac{\partial \mathbf{J}}{\partial t} + \epsilon_0 \frac{\partial^2 \mathbf{E}}{\partial t^2} = \frac{-1}{\mu_0} \bigtriangledown \times (\bigtriangledown \times \mathbf{E}). \tag{2.13}$$

Now, we know that the electrons will move according to Newton's Second Law,

$$m_0 \dot{\mathbf{v}} = -e\mathbf{E}, \tag{2.14}$$

where $\dot{\mathbf{v}}$ is the the acceleration.The definition of $\mathbf{J}$ is,

$$\mathbf{J} = -Ne\mathbf{v}. \tag{2.15}$$

Taking a time derivative here and plugging in the Equation 2.14 will leave us with,

$$\frac{\partial \mathbf{J}}{\partial t} = \frac{Ne^2}{m_0} \mathbf{E}.$$

Substituting this into Equation 2.13 and dividing by ϵ_0, we notice that the coefficient on E is ω_p^2. This then leaves us with,

$$\omega_p^2 \mathbf{E} + \frac{\partial^2 \mathbf{E}}{\partial t^2} = -c^2 * \bigtriangledown \times (\bigtriangledown \times \mathbf{E}). \tag{2.16}$$

It now adds intuition to this scenario to split $\mathbf{E}$ into a sum of its longitudinal and transverse components, such that $\mathbf{E} = \mathbf{E}_t + \mathbf{E}_l$ that are subject to the conditions $\bigtriangledown \times \mathbf{E}_l = 0$ and $\bigtriangledown \cdot \mathbf{E}_t = 0$. These conditions arrive from solutions to the boundary conditions at a dielectric interface. Inserting these into Equation 2.19 and applying a vector identity and rearranging gives,

$$\omega_p^2 \mathbf{E}_t + \frac{\partial^2 \mathbf{E}_t}{\partial t^2} - c^2 \bigtriangledown^2 \mathbf{E}_t = -\left(\frac{\partial^2 \mathbf{E}_l}{\partial t^2} + \omega_p^2 \mathbf{E}_l \right). \tag{2.17}$$

We see we are left with an equation solvable by separation of variables. The constant turns out to be zero, giving us two homogenous equations,

$$\omega_p^2 \mathbf{E}_t + \frac{\partial^2 \mathbf{E}_t}{\partial t^2} - c^2 \bigtriangledown^2 \mathbf{E}_t = 0, \tag{2.18}$$

$$\frac{\partial^2 \mathbf{E}_l}{\partial t^2} + \omega_p^2 \mathbf{E}_l = 0. \tag{2.19}$$

The left hand side is a form of the Helmholtz equation and the right hand side is a simple harmonic oscillator. These oscillating electric fields arising from the fluctuating charge densities are plasmons, as seen in Figure 2.4a. From these last two equations we see that we have two fields that can exist in a plasmon. This distinguishes the two different types of electric fields, both of which can solved with wavelike solutions of the functional form $e^{i(\mathbf{k}\cdot\mathbf{r}-\omega t)}$. We search for solutions of the form $e^{i\mathbf{k}\cdot\mathbf{r}-\omega t}$. For a transverse wave we find we are restricted to solutions where,

$$\omega^2 = \omega_p^2 + c^2 k^2, \tag{2.20}$$

which is the dispersion relation for a plasmon. Equation 2.19 has the wave solution bound by the condition,

$$\omega = \omega_p. \tag{2.21}$$

So we see that we have two different forms oscillations capable in these materials, one kind is in the transverse electric field and one in the longitudinal electric field.

Figure 2.4: a) Graphic depicting the oscillating charge density and corresponding electric fields that constitute a plasmon. Image credit to [25]. b) Image of an AFM using s-SNOM to launch plasmons. The plasmons can be measured by interfering them with their reflection off of boundaries. Image credit to [26].

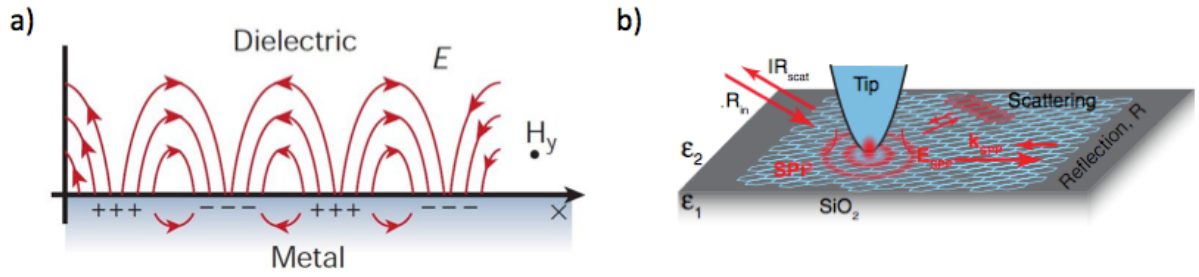

In metals, bulk plasmons and surface plasmons can exist, both of which are governed by the above equations. Bulk plasmons can only exist as longitudinal fields and surface plasmons arise from both a longitudinal and a transverse electric fields [24]. If these systems couple to a photon the result is a surface plasmon polariton (SPP). These nanoscale fields propagate at the surface of a material and can be directly observed in real space with interferometry achievable through s-SNOM, Figure 2.4b. The high momenta of the fields produced during s-SNOM can satisfy the dispersion relation in Equation 2.20. These oscillations decay away from the AFM tip, but when close to an edge or boundary, these waves can be reflected and measured. Measurements of this will be discussed in Chapter 4.

2.3 Spontaneous Raman scattering

Raman spectroscopy has proven to be useful in the study of 2D crystals [11]. In these inelastic scattering processes, incident photons interact with vibrational modes in the structures, resulting in the emission of a photon that is shifted in energy by an amount related to the energy of the phonon [24]. Due to the inelastic and spontaneous nature of these interactions, the efficiency of the process is quite low; roughly one in a million photons will experience the shift [11]. The invention of the laser as well as the use of confocal Raman microscopy has increased the sensitivity of this

technique, but signals are generally quite low, especially relative to the incident laser light[24]. By using a low pass optical filter that cuts off steeply below the laser line, a series of peaks can be observed corresponding to the different normal modes of oscillation in the lattice. The response is incredibly sensitive to very small changes in the lattice, easily identifying different phases, stacking orders, thickness, and even composition [11]. In the case of 2D materials, the number of atomically thin layers alters present affects the Raman spectrum, making Raman scattering an ideal method for identifying the thickness of a sample. The changes in spectrum are limited to being able to distinguish up to ten or so layers, after which the crystal exhibit a bulk response.

2.3.1 Phonon modes

Phonons are quasi-particles that arise in matter as the result of collective oscillations in a crystal lattice [24]. Materials have both optical and acoustic phonons. Optical photons are characterized by the motion of adjacent atoms being out of phase whereas for acoustic phonons, the oscillations are in phase. To conceptualize this idea, we can think of a crystal as an array of coupled oscillators. Classically for this system we can derive the Lagrangian and apply the Euler-Lagrange constraints on the system, leaving us with a set of linear equations whose solutions are the set of normal modes of oscillations. These oscillations would corresponded to the phonons and the calculated frequencies of the normal modes are the phonon frequencies. In this coupled oscillator system, the frequency of these varies depending on the weights attatched and the arrangement of the spring. This same concept holds true for the phonon modes in crystals. Different structures will have unique modes with unique corresponding frequencies. These modes then provide a potential method for identifying materials.

2.3.2 Stokes shifts

The material fingerprinting ability of materials in Raman spectroscopy relies on the intensities and positions of phonon interaction peaks relative to the incident light [11]. The position of the peaks relative to the incident light is known as the Stokes or Anti-stokes shift and is described

mathematically as,

$$\omega_1 = \omega_2 \pm \Omega, \tag{2.22}$$

where ω_1 is the measured signal, ω_2 is the incident frequency, and Ω is the shift in the frequency. The plus sign corresponds to the emission of a phonon and a Stokes shift and the minus sign corresponds to the absorption of a phonon, an Anti-Stokes shift. If working with wavelength, this corresponds to an increase in wavelength for the stokes shift and a decrease in wavelength for the Anti-stokes shift [24]. These shifts, Ω, can always be identified at the exact same position using units of relative wavenumber. We can calculate this using the equation,

$$\nu = \frac{1}{\lambda_{incident}} - \frac{1}{\lambda_{scattered}}. \tag{2.23}$$

This allows us to always position these peaks at identical spectral positions regardless of the illumination source. If we have highly accurate measurements of these spectra we can then identify different phases and thicknesses based upon slight variations in the peaks. The spectrum can change by having alterations in relative peak intensities, shifts in frequency, peak splittings, peaks developing shoulders, and broadening depending on the material being studied.

2.4 Scanning probe microscopy

Scanning probe microscopy(SPM), is a form of nanoscale imaging that utilizes a nanoscopic tip as opposed to light. In the early 1980's, the first form of scanning probe microscopy was invented, the scanning tunneling microscope (STM) [13]. We see a diagram of this in Figure 2.5c. By placing a metallic tip with a radius of a few nanometers very close to the sample and applying a voltage bias between them, a current can be measured as the electrons tunnel between the tip and sample. Piezoelectric stages are used in order to control the tip position. Piezoelectric materials experience a reproducible expansion when a voltage is applied to them, allowing for precision positioning and measurement on the scale of tens of picometers. Using a P.I.D feedback loop, the

tip's z-axis location could be altered to maintain a steady current. By raster scanning the probe over the sample, the electron density can be mapped out. However, this system only works well for materials with high electron mobility. Additionally, the presence of any non-conducting debris on the sample is destructive to the soft metal tips, blunting or destroying them since no feedback current is received over the debris.

Figure 2.5: Diagram of basic concept behind the scanning probe microscopy methods of a) tapping model with photodiode detection b) a tuning fork shear force system c) a scanning tunneling microscope

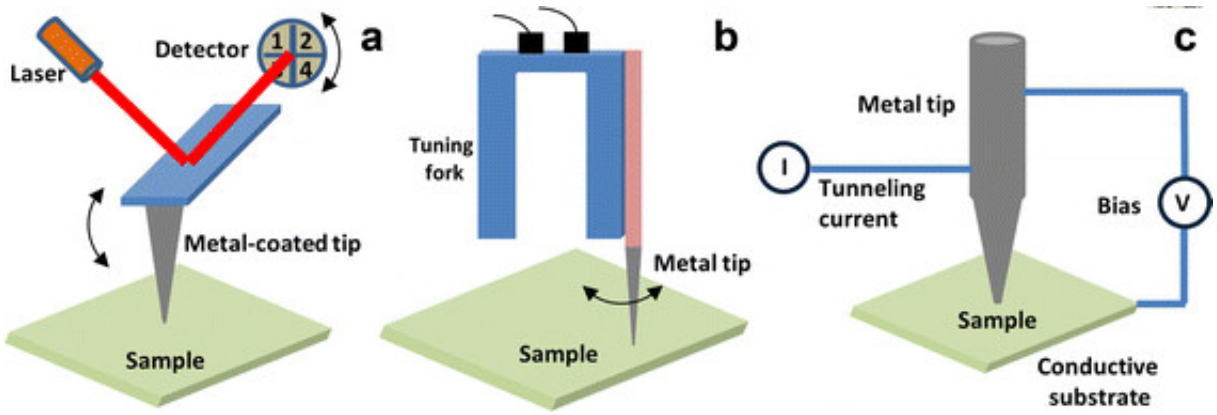

After that, a shear force form of scanning probe microscopy, Figure 2.5b, was created [13]. This involved taking a similar nanoscopic tip and placing it on a quartz tuning fork. The tuning fork and tip are driven near resonance by an oscillating piezo. When the tip approaches the sample these oscillations are damped, causing a shift in frequency or amplitude of the tuning fork motion that can be measured and used to modulate the tip-sample distance and map the topography. The tip position is also controlled through the use of piezoelectrics. The underlying mechanism behind the tip sample interactions in shear force is still unclear, though various models have been proposed. However, the technique still has been proven to be effective at imaging nanometer scale systems [27].

The third type of scanning probe microscopy I will discuss is a tapping mode AFM system, Figure 2.5a. In this form, the nanoscopic tip is mounted to a cantilever with a well-defined res-

onance. A laser illuminates the backside of the cantilever and is reflected onto a four-quadrant photodiode. As the tip moves up and down the amount of light that reaches the photodiode varies. By measuring the position of the reflected beam on the photodiode, an image can be constructed in order to obtain nanoscale images. Unlike STM and shear force, this method involves direct contact with the sample. To accommodate this, the tips of tapping style AFM's are usually made of a more robust material than those in shear force and STM systems.

2.5 Near-field optics

The near-field is a region close to the surface of a sample in which electric fields exists as nonpropogating evanescent fields. To describe this we start by having an electromagnetic wave with a purely real wave vector $\vec{\mathbf{k}}$. However, near the surface, $\vec{\mathbf{k}}$ becomes complex, $\widetilde{\vec{\mathbf{k}}}$, with its imaginary component perpendicular to the surface. This imaginary component prevents observation in the far-field as the field decreases in strength exponentially as you move further from the surface. However, these fields also have high spatial resolution as we now have an evanescent field that is no longer bound by the diffraction limit because it is no longer wavelike in nature. It is important to note that momentum in this situation is still conserved and so $\|\widetilde{\vec{\mathbf{k}}}\| = \|\vec{\mathbf{k}}\|$. To make this true, we must have an increase in the in plane vector components $\widetilde{k}_x$ and $\widetilde{k}_y$ in order to compensate for the imaginary $\widetilde{k}_z$ component. This means that in the near-field we have very high in plane momentum. These high momenta can be used to excite states such as plasmons that are not accessible with far-field light.

2.5.1 NSOM

Near-field scanning optical microscopy (NSOM) was the first technique to achieve sub-diffraction limited optical spectroscopy. In this method, depositing a metallic coating around an optical fiber forms a nanoscale aperture [13]. The sample is illuminated through the fiber and then the tip is raster scanned over the surface, allowing the aperture to collect the evanescent electric field. The field then moves through the fiber and into an optical cable that then feeds into a detec-

tor [11]. This process is modeled in Figure 2.6. While effective, this method has several drawbacks. The tips are difficult to fabricate reproducibly. Additionally, there is a trade off between the signal magnitude and the spatial resolution [13]. To increase the spatial resolution of the probe one must decrease the size of the aperture of the fiber, but by doing so, they decrease the amount of signal that could be collected as well. Additionally, the signal scales as $\frac{1}{\lambda^4}$, limiting the effectiveness of this process for low energy processes. Ultimately, the resolution of this method is limited to 50-100nm [11].

2.5.2 s-SNOM

NSOM was the first method to achieve sub-diffraction limit spatial resolution in optical fields. However, the trade off between resolution and signal strength was not ideal. Scattering-type scanning near-field optical microscopy (s-SNOM) is a method that delivers an increase in signal strength as the resolution increased [11]. By focusing light onto the apex of an atomic force microscope, see Figure 2.6, a highly localized non-propagating electric field is formed. As this field is no longer wave-like in nature, it is no longer diffraction limited. This gives us the ability to have a highly localized field on the nanoscale. The tip also acts as a local scatterer, which can then scatter the light back into the far-field. The radius of the tip at the apex determines our spatial resolution and also the strength of our field, both of which increase with a decreasing tip radius[11]. Conveniently, this method does not require an aperture to collect the light. This means that we no longer have a trade-off between an increase in spatial resolution and signal and we are limited only by our tip radius[11]. At infrared wavelengths, spatial resolution can be more than a factor of 1000 times higher than would be allowed by the diffraction limit.

One of the main issues that arises in s-SNOM is a large far-field background. Typically a parabolic mirror is used to focus light onto the apex of the atomic force microscope. The focus of the light is usually several microns in size, depending on the wavelength and alignment, and the tip is several nanometers in size. This means that the near-field information from the tip is dominated by the far-field signal from the excitation of the area around the tip. In order to identify

Figure 2.6: We see diagrams of NSOM and s-SNOM. Notice the NSOM technique does not excite a large background area as the excitation is confined to the inside of the probe. This contrast to s-SNOM where a larger area of the sample is illuminated.

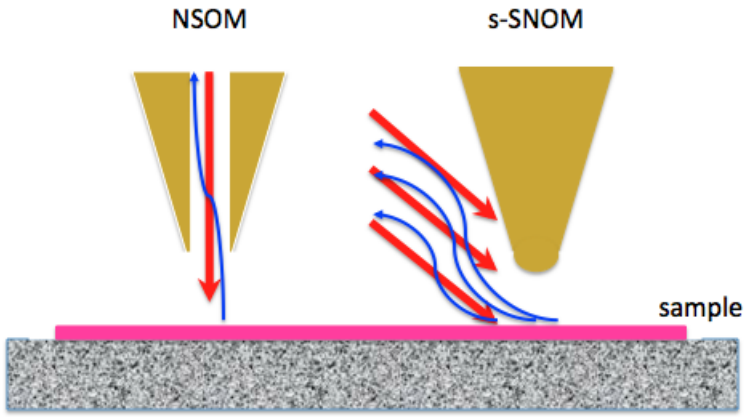

the near-field signal one must first remove the far-field background. This is usually accomplished through lock-in amplification. Various methods have been developed for this, which I will discuss in chapter 3.

2.6 Simple coupled dipole model of tip sample interactions

The complete description behind the tip-sample interactions in s-SNOM is not fully understood to date. However, several basic descriptions exist that provide an intuition for the process. Among these, the point dipole approximation is the simplest. Due to the finite radius of the scattering tip and the distance of the shaft being greater than that of the tip, we can approximate the probe as a sphere with radius a [11]. Based on this, we model the tip as a polarizable sphere, with dielectric function ϵ_{sph}, with its center a distance d from a grounded plane with a complex dielectric, ϵ_{surf}. Applying an external electric field, $\mathbf{E}$, will create a polarization in the sphere,

$$\mathbf{P} = \overleftrightarrow{\alpha}_{sph}\, \epsilon_0 \mathbf{E}, \tag{2.24}$$

where $\overleftrightarrow{\alpha}_{sph}$ is a tensor defined as,

$$\alpha_{sph,ij} = 4\pi r^3 \frac{\epsilon_{sph} - 1}{\epsilon_{sph} + 2} \delta_{ij}.$$

Figure 2.7: Image representation of a) the polarization of the tip and the image charge in the coupled dipole model with incident electric field solely in the z-direction. b) Plots of the varying signal achieved between Au and Si samples that accounts for the contrast observed in the near-field signal. Image credit to [11].

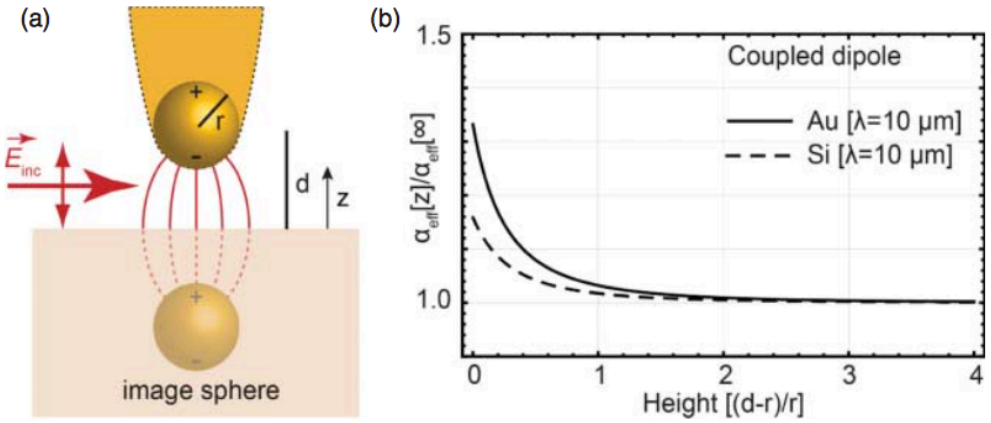

This accounts for the various polarizations that can be induced. I will only discuss a field perpendicular to the surface, $\mathbf{E} = E_z$. This will create a dipole in the sphere with a positive charge furthest from the sample and a negative charge on the side closer to the sample. The dielectric plane then has an induced surface charge. The corresponding electric fields present in this scenario can be solved by the method of image charges, allowed by the uniqueness theorem. The image charge is introduced as a sphere embedded in the dielectric sample at a distance $-d$ with an identically-induced polarization and relative strength given by $\beta = \frac{\epsilon_{surf}-1}{\epsilon_{surf}+1}$. This leaves us with an effective polarization in the z direction described by,

$$P_{z,eff} = \alpha_{z,sph}\left(1 + \frac{\alpha_{z,eff}\beta}{16\pi d^3}\right)\epsilon_0 E_z. \tag{2.25}$$

The β term in this equation results in a coupling between the dielectric function of the tip and the dielectric function of the sample, as seen in Figure 2.7. The result is that the scanned

surface's dielectric function affects the polarization and because of the constant dielectric of the tip, the alterations in the polarization are solely from the sample, creating a contrast in the signal between varying samples[11]. In Figure 2.7b, this contrast is modeled mathematically between Au and Si with a 10 μm illumination source. We see varying signal between the two subsances. The field resulting from these coupled dipoles constitutes the evanescent field that is used as a probe in s-SNOM. These fields also have a momentum associated with them that is functionally proportional to $\frac{1}{a}$ [28]. This is an important aspect as we can then use these fields to excite states that are not accessible merely with light, such as plasmons.

Chapter 3

Methods

3.1 Raman spectroscopy setup

In the Raman spectroscopy setup there are two lasers for excitation, a 532 nm diode laser that shows a power output of 10mW and 632.8 nm HeNe gas laser that outputs 21 mW. The 532nm beam is expanded through a telescope consisting of two anti-reflection coated lenses to enlarge the beam diameter by a factor of six. The 632.8nm laser remains unexpanded as it is easier to align without the telescopes. Both beams are aligned colinearly and directed into an optical microscope in order to have an identical focal spot so that they can both be used without realignment of optics. The objectives used for magnification of the sample are also used to focus the beams onto the sample in order to stimulate Raman interactions. The same objective is used to collect the back-scattered signal from the sample. Since the backscattered light is slightly divergent after exiting the objective. We use an anti-reflection coated lens for collimation. The light passes through a steep low pass filter that cuts out the incident laser light, allowing the Raman response to be detected by the spectrometer. The overall schematic can be seen in Figure 3.1. The green line represents the excitation beam and the red line represents the signal.

The spectrometer we use is a Princeton Instruments Acton SP2500. It has an adjustable slit that is focused onto by an exterior lens. The light entering is dispersed by a grating and then detected on a liquid nitrogen cooled CCD.

Figure 3.1: a) Photograph of the Raman spectroscopy setup overlaid the laser line and b) experimental schematic of Raman spectroscopy setup

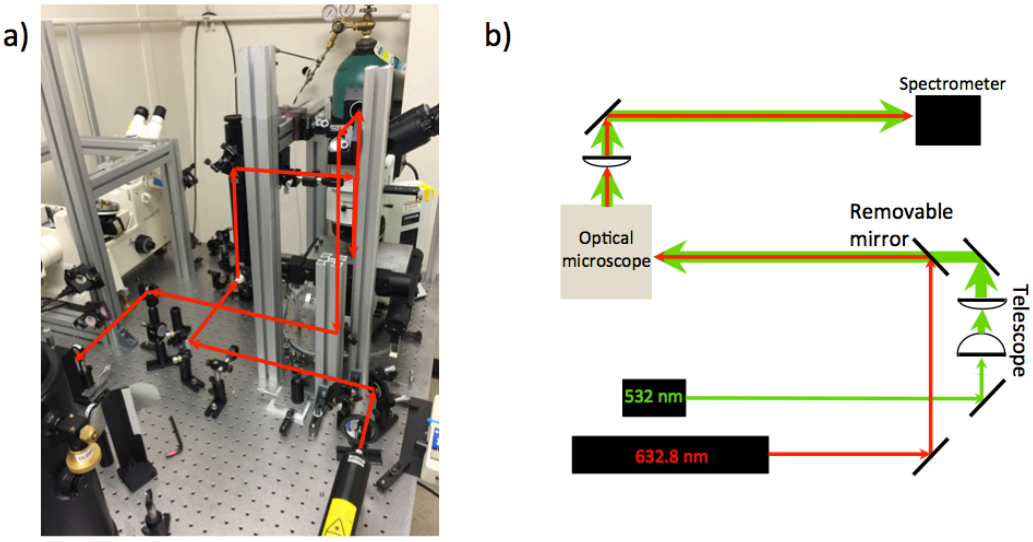

3.1.1 Raman lab Optimization

In order to improve the sensitivity of the Raman spectroscopy setup, I developed a component by component process to assess the amount of signal intensity loss in each component. Using a power meter and UV-Vis spectroscopy we noticed several locations in the setup that were drains for signal. Several mirrors were replaced which increase the signal by 10%. I also discovered that several of the anti-reflection coated lenses in the system were cutting upward of 30% of the signal from our 532nm laser. These were replaced with broadband anti-reflection lenses, 350nm-1000nm, to reduce loss in both lasers and their signals. These alterations gave us an increase in signal by a factor of about 2.5. Additionally, a beam expander was added to decrease the focal spot size of laser light. While the original intention of this was to increase spatial resolution of the scan, the signal was increased substantially. The results of the optimization are demonstrated in Figure 3.2, where we see an increase in signal by nearly an order of magnitude as well as an increase in signal to noise of around three.

The next step was to increase the stability of the system. I replaced a telescope made of

Figure 3.2: Raman spectrum a) before component optimization with 10 s exposure time b) after optimization with 1 s exposure. We see that the new spectrum is of comparable quality, but the optimized spectrum took a tenth the exposure time.

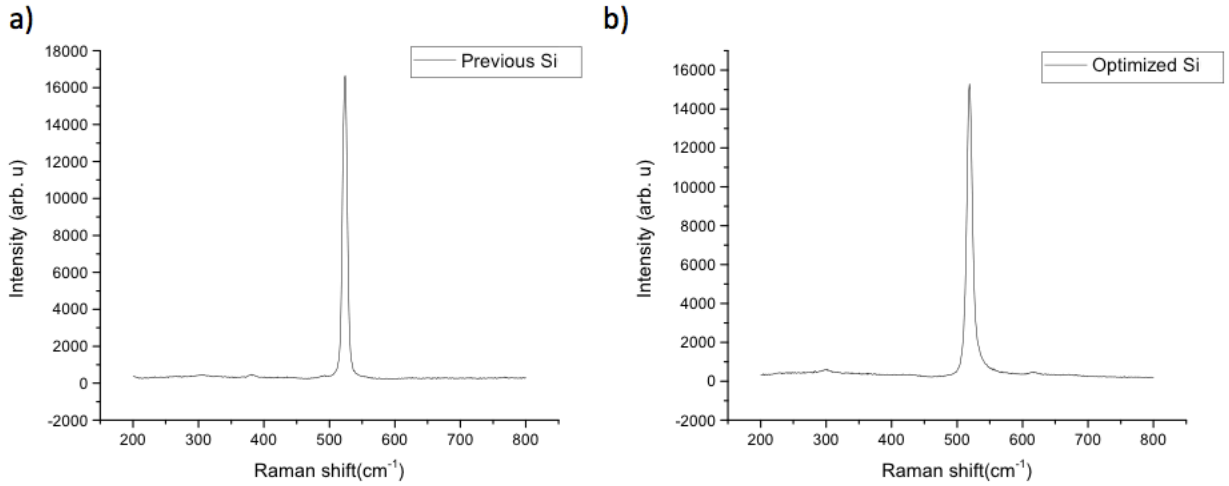

extruded aluminum tubing with a solid milled tube. This increased the lateral mechanical stability as it could be more strongly secured to the table, reducing vibrations and drift. Additionally, I discovered that the heat output from the microscope lamp caused substantial amounts of thermal instability. To further increase the stability of the setup, I adjusted the procedure to minimize the amount of time that the lamp was on. However, the greatest alteration to the system was its enclosure. The room has strong air currents generated from an air conditioning unit that resulted in substantial drift laterally as well as in in the z-direction. Therefore, a frame was machined out of extruded aluminum tubing. The roof was cut from a sheet of black PCV. Black curtains were added in order to reduce stray light contamination in the signal and to reduce the air currents but still allow for easy access to the setup. A final image of the setup can be seen in Figure 3.3. Overall, these adjustments increased the stability of the setup from several minutes to more than 12 hours for the z direction and 2-3 hours for the lateral position.

Overall, we saw an increase in the Raman signal by almost an order of magnitude and a

Figure 3.3: Photograph of the covered Raman lab setup. A frame was constructed out of extruded aluminum for the housing. A PCV roof was constructed to the dimensions of the optics table and black out curtains were bought to cover the open sides.

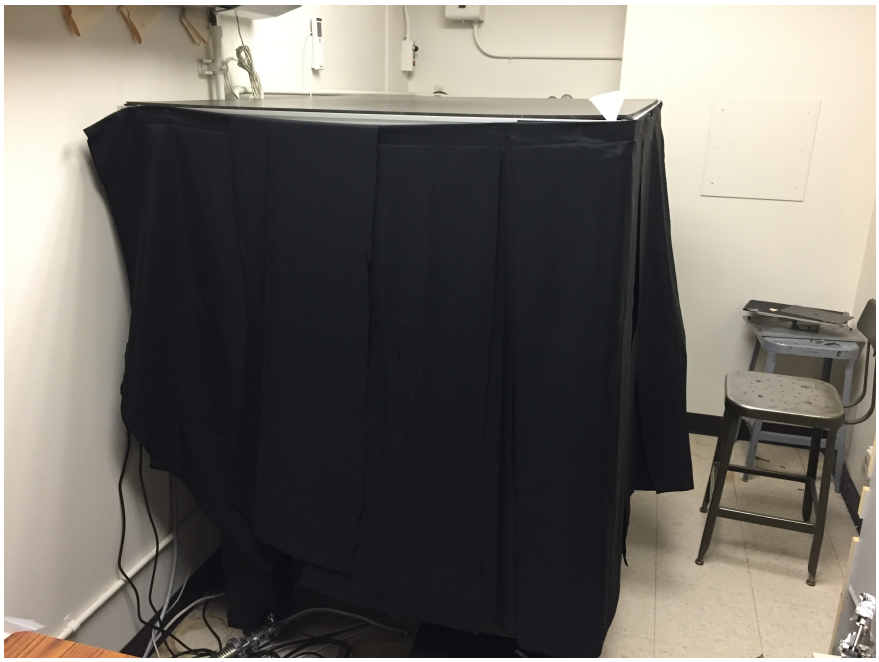

drastic increase in the stability of the system.

3.1.2 Development of an an experimental setup for line scan Raman Spectroscopy

In order to gain insight into the edge states of transition metal dichalcogenides, we decided that a line Raman scan would be preferable to the usual point spectroscopy measurements. To realize such an experiment, it was important to have a high level control of the microscope stage. This involved the replacement of the conventional hand controlled microscope translational stage with an electronic stepper motor stage with an increased precision. The stage can be controlled with ASCII commands input from a computer. Using this stage, we can achieve steps of sizes with a lateral resolution of about 1 micron. The previously mentioned improved stability and the achieved order of magnitude increase in signal were a crucial factor in being able to reproducibly perform Raman line scans. The improvements I made allowed for quick and stable line scans.

3.2 Scattering-type Scanning Near-field Optical Microscopy

The basic principal of s-SNOM is to focus laser light onto the apex of an atomic force microscope. In order to focus our 10.8 μm light on to the apex of our probe, we use an Au-coated off axis parabolic mirror (OAPM) mounted to a translational stage. The stage has coupled y- and z- axes. The same mirror collects the back scattered light from the tip that constitutes our signal.

The signal is detected with a Mercury Cadmium Tellurium detector (MCT). This incident light on the detector produces a current that corresponds to our near-field signal. The detected signal from the setup contains both far-field and near-field data. Various methods exist for the treatment of the signal in order to optimally extract the near-field information[11].

In our experiments, we use a tapping mode setup for our AFM. In order to extract higher near-field data from the large far-field background, we use a lock-in amplifier for detection. Near-field data can only be acquired when the tip-sample distance is less than one wavelength distance from the sample. Since the tip is oscillating, the near-field signal only exist at the same frequency of oscillation. Therefore, we only wish to detect signal at the same frequency of oscillations as the tip. We use a lock-in detector, a Zurich HF2LI, to demodulate the signal only at the harmonics of the tip frequency. It is preferable to detect at higher harmonics, as this gives us a better isolation of the actual near-field response [11]. This can be thought of as using a more terms in your Fourier transform of the signal, which gives us a better fitting to the actual near-field response, allowing for a better filtration of the far-field signal.

3.2.1 Two-phase homodyne s-SNOM

There are several detection schemes commonly used in s-SNOM. They are self-homodyne, and two-phase homodyne. They different types of interferometry that can be used in order to sample out the background signal from the actual near-field signal and extract phase information. I will briefly describe self-homodyne measurements, as it lays the foundation for two-phase homodyne detection, which I will do an in depth analysis of.

Figure 3.4: Basic schematic for self-homodyne detection in s-SNOM.

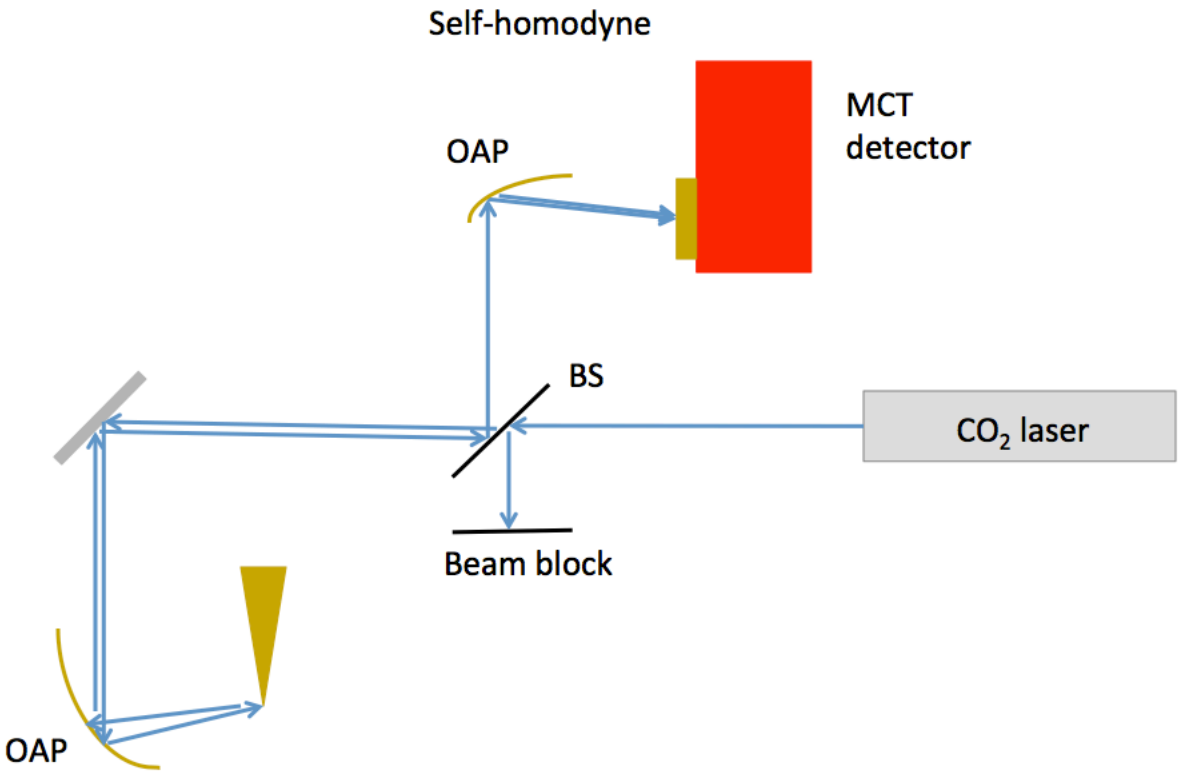

In self-homodyne detection, the laser light passes through a beam splitter with one beam going to the sample while the other is directed to a beam block. The backscattered signal from the sample is collimated by the OAMP and goes back up the beam path, reflecting off the beam splitter and entering the detector. This method gives near-field information but is highly limited as it does not give phase information and lacks the interferometric amplification of a reference arm.

In contrast, homodyne detection utilizes an asymmetric Michelson interferometer that includes a reference arm. The end mirror of the reference arm is attached to a piezo that can be used to control its positioning with nanometer accuracy. In this scenario, we have three distinct fields interfering on the detector, the near-field signal E_{nf}, the far-field signal E_{ff}, and the reference arm signal E_{ref}. Hence, the detector ultimate measures the intensity,

Figure 3.5: Basic schematic for homodyne detection in s-SNOM.(OAP, off-axis parabolic mirror; BS, beam splitter; MCT, Mercury Cadmium Telluride detector)

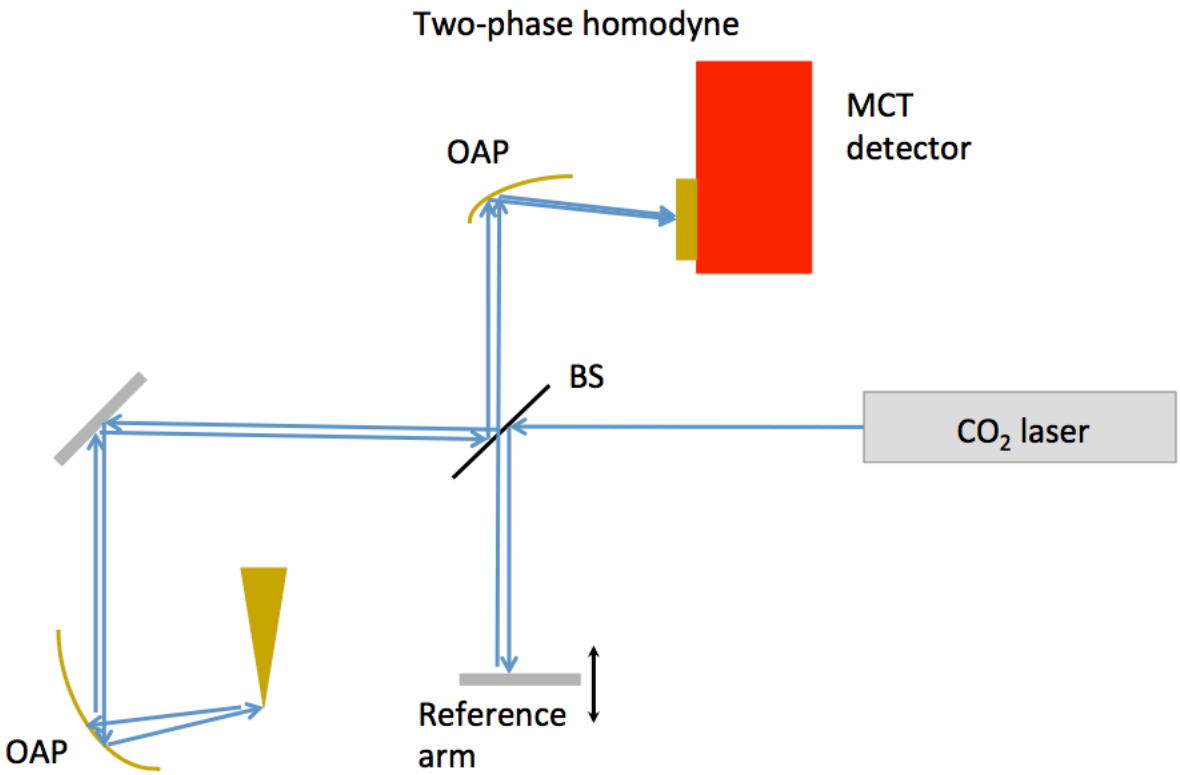

$$I_{tot} \propto E_{tot}E^*_{tot} = (E_{nf} + E_{ff} + E_{ref})(E^*_{nf} + E^*_{ff} + E^*_{ref}), \tag{3.1}$$

which is equal to,

$$I_{tot} = \|E_{nf}\|^2 + \|E_{ff}\|^2 + \|E_{ref}\|^2 + E_{nf}E^*_{ff} + E_{nf}E^*_{ref} + E_{ff}E^*_{nf} + E_{ff}E^*_{ref} + E_{ref}E^*_{nf} + E_{ref}E^*_{ff}.$$

Because $\|E_{nf}\|^2$ is small relative to the other terms, it can be approximated to be zero. All of the terms that do not contain $\|E_{nf}\|^2$ or its conjugate can also be ignored as they are eliminated by lock-in detection. This leaves us with,

$$I_{tot} \propto E_{nf}E^*_{ff} + E_{nf}E^*_{ref} + E_{ff}E^*_{nf} + E_{ref}E^*_{nf}.$$

Of these terms, those with a E_{ref} dominate, because $E_{ref} \gg E_{ff}$. This leave us with,

$$I \propto E_{nf}E^*_{ref} + E_{ref}E^*_{nf},$$

which can be rewritten as,

$$I \propto 2\|E_{nf}\|\|E^*_{ref}\|\cos(\phi), \tag{3.2}$$

where ϕ is the phase difference between the signal and the reference arm. Recalling that in the setup, we have control of the positioning of the reference arm. This allows varying the phase in a controlled manner. In two-phase homodyne, we can pick a location for two positions of phase that differ by $\frac{\pi}{2}$. The $\frac{\pi}{2}$ phase difference can be achieved by moving the mirror a distance of $\frac{\lambda}{8}$, as $\frac{\pi}{2}$ phase would correspond to a $\frac{\lambda}{4}$ difference in length, but the beam propagates twice the distance the mirror moves. Doing this will give a pair of intensities,

$$I_1 \propto 2\|E_{nf}\|\|E^*_{ref}\|\cos(\phi)$$

$$I_2 \propto 2\|E_{nf}\|\|E^*_{ref}\|\cos(\phi + \frac{\pi}{2}).$$

Subbing in for $\cos(\phi + \frac{\pi}{2}) = \sin(\phi)$ leaves us with,

$$I_1 \propto 2\|E_{nf}\|\|E^*_{ref}\|\cos(\phi),$$

$$I_2 \propto 2\|E_{nf}\|\|E^*_{ref}\|\sin(\phi).$$

If we divide these two equations, we get,

$$\frac{I_2}{I_1} = \tan(\phi).$$

By taking the inverse tangent of both sides, we find we can solve for the phase from these two fields,

$$arctan(\frac{I_2}{I_1}) = \phi. \tag{3.3}$$

If we take the sum of the squares of the two intensities we find,

$$I_1^2 + I_2^2 = 4\|E_{nf}\|^2\|E_{ref}^*\|^2\cos^2(\phi) + 4\|E_{nf}\|^2\|E_{ref}^*\|^2\sin^2(\phi)$$

$$= 4\|E_{nf}\|^2\|E_{ref}^*\|^2 \propto \|E_{nf}\|^2$$

Through this method we can fully resolve the optical near-field response in amplitude and phase, making it a powerful tool for assessing optical conductivity or dielectric properties on the nanoscale.

Chapter 4

Experiment and results

My work focused around two main projects. The first of these experiments was investigating graphene stacking order boundaries in bilayer graphene. This was part of a collaboration with Pennsylvania State University professor Jun Zhu. They hoped to build electronic devices on these boundaries, which have been shown to exhibit increased carrier densities and other interesting properties [8]. We investigated using s-SNOM to identify these boundaries. Additionally, during these measurements, we repeated the experiment performed by Gerber *et al*, involving plasmon interferometry off of the edges of these bilayer graphene sheets and experimented with the possibility of using plasmon interferometry to investigate the stacking order defects identified with s-SNOM.

The second project involved studying of two phases of $MoTe_2$, the semiconducting 2H phase and the conducting 1T' phase. We were interested in investigating an optically induced phase transition reported by Cho *et al*[14]. In their report, they began with samples of the 2H structure of the crystal and found that by focusing high intensity light onto it, they could ablate the structure down to a single monolayer and shift the lattice structure into the conducting 1T' phase [14]. They measured Raman spectra of the new states and then identified the cause of the transition to be Te vacancies in the lattice. I reproduced these results with our own Raman set up and characterized both states. To further assess this transition, we performed s-SNOM measurements with 10.8 μm light on the transitioned areas. As neither of the 2H and 1T' phases have been explored using s-SNOM, this also proved an excellent opportunity to explore the properties of the unaltered of the materials. In this work, I collaborated with a staff scientist at NIST, Samuel Berweger, who

provided samples and complementary data on the near-field interactions of microwaves with these materials.

4.1 Graphene grain boundary detection and plasmonic interferometry

Figure 4.1: Structural representations of the AB (left) and AA (right) stacking orders for bilayer graphene. Image credit to [29]

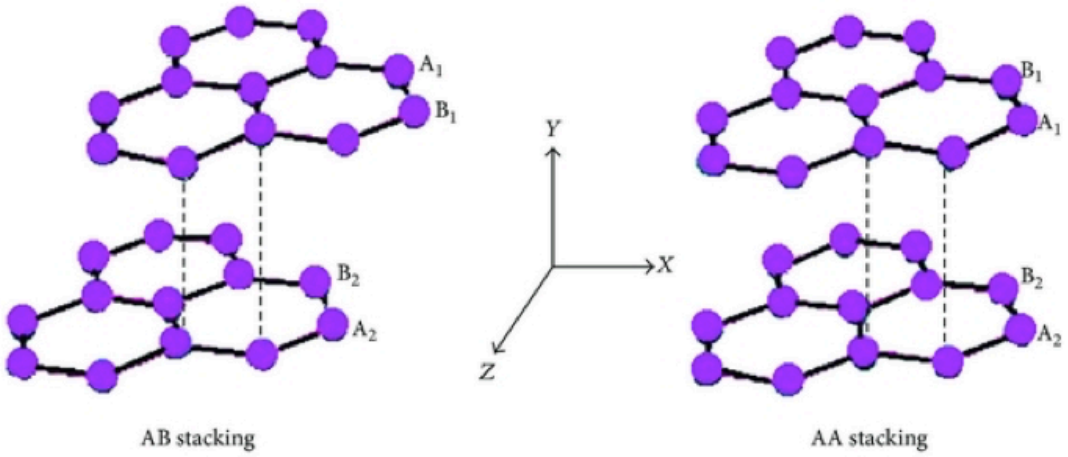

In Figure 4.1, we see the stacking orders of bilayer graphene. The two different states are distinguishable by the relative positions of the atoms in the two sublattices. Additionally, inversions of both of these orders can exist. Rotating π radians around the x-axis of the AB orientation leads to BA stacking. Rotating the AA lattice around the x-axis produces an indistinguishable lattice, therefore no BB lattice exists. When switching from one stacking order to another, particularly an AB-BA transition, an alteration in the lattice occurs [8]. These stacking boundaries are of high interest for the manufacturing of micro-devices, as they have been shown to have high carrier densities and increased conductivity [8]. These are the stacking order grain boundaries we sought to identify. We implemented self-homodyne s-SNOM in order to detect these boundaries. Exfoliated bilayer graphene samples were provided through a collaboration with Jun Zhu from Pennsylvania State University.

Figure 4.2: Two-phase homodyne s-SNOM images of a bilayer graphene flake. We have images of the a) topography of sample , b) near-field amplitude measurements, c) near-field phase measurements , d) amplitude line cut profiles, and e) phase line cut profiles. The lines in the images correspond to the line cuts that are represented in figures d) and e).

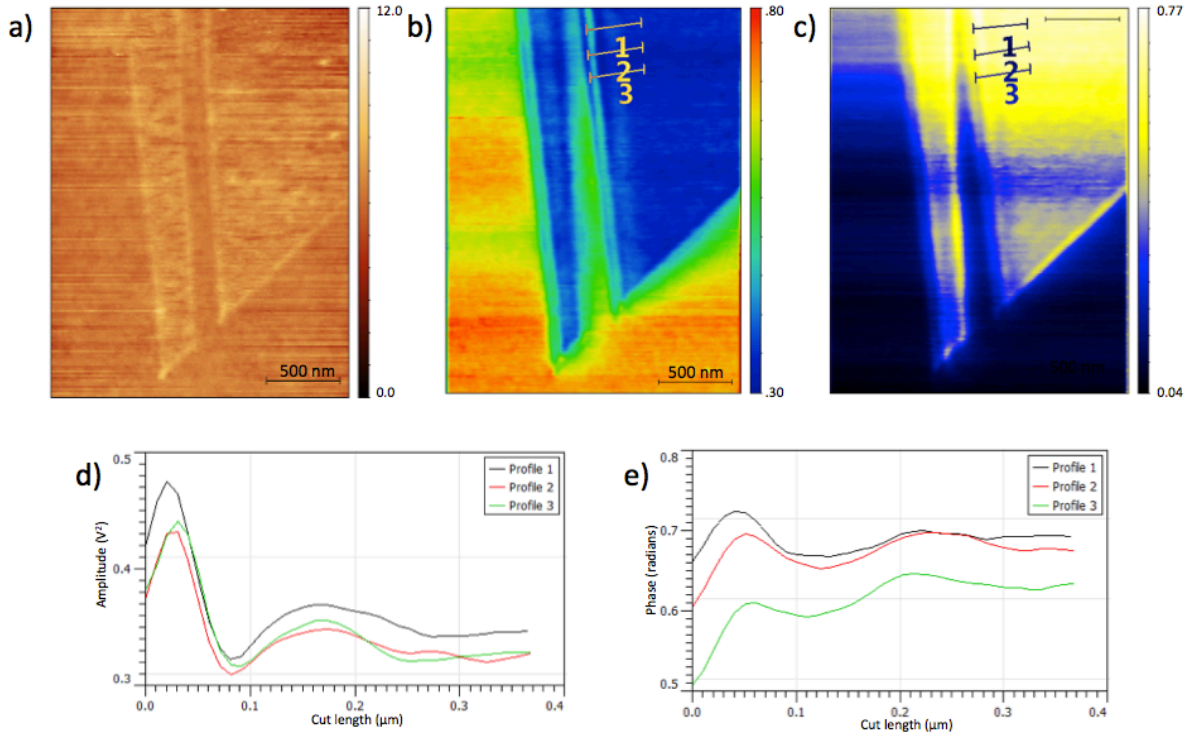

4.1.1 Plasmon interferometry reconfirmation of results

We repeated the experiment of Gerber *et al* on our provided graphene samples. 2-phase homodyne detection was utilized in order to gain full phase resolution of these oscillations. The edges of these crystals should show an interference pattern resulting from counter propagating plasmons launched from the tip. Figure 4.2 shows the topography, s-SNOM signal amplitude, and phase, as well as line cuts from the amplitude and phase. The amplitude measurements assess the magnitude of the electronic response of the material at IR wavelengths. Practically these are images that are measures of the Fermi level and conductivity. The phase measurements can be thought of as a measure of the delay of the electronic response from the material. We measured the decaying oscillations over 300 nm, which was consistent with previous measurements and predictions [26].

However, we did notice that the wavelength varied throughout the decay in the phase. This is seen clearly in line cut plots of the amplitude and phase, Figure 4.2d-e. This effect may result from variation in the charge densities through the area. Recalling Equation 2.7, we notice that plasmon frequency is proportional to the root of the electron density. Charge density has been proven to cause changes in the plasmon wavelength [30].

We implemented s-SNOM on bilayer graphene samples as described by [8] in order to identify stacking order defects. The identification of these defects in these materials would be characterized by a change in the amplitude and phase in self-homodyne s-SNOM. We scanned over several areas that were roughly 10μm by 50μm with s-SNOM using the same 10.8 μm light as used for the previous edge experiment we conducted. Figure 4.3 exemplifies one of our results. In 4.3a we see that the topography of the scanned area does not show any obvious boundary, yet in 4.3b we notice that there is a shift in the amplitude of the optical signal, moving from the top center-right to the bottom center-left. The lack of topographic sign but the shift in the optical signal are the reported signs of these boundaries [8]. No oscillations were observed as we were using a self-homodyne detection scheme, meaning we did not have full phase data, and also due to the weakness of the boundary, which allows for high transmission of the plasmon. Future measurements were taken on other crystals with a two-phase detection pattern that did observe the interferometric fringes similar to what we observed on the edges in Figure 4.2. This could be expected, as we had previously shown that we could excite plasmons near the edges of the structures and the stacking order defects found in graphene present similar boundaries to those edges, making them a possible locations for the interferometry of surface plasmons.

Boundaries like these were identified on numerous graphene samples using both self-homodyne and two-phase homodyne methods. The results were shared with our collaborators and they are currently taking the samples and attempting to build devices. This work will be resumed after they finish fabricating the devices and performing their own measurements.

Figure 4.3: s-SNOM images of a bilayer graphene grain boundary. We see the a) topography and the b) near-field signal. Notice the appearance of the boundary in the optical signal but not the topography.

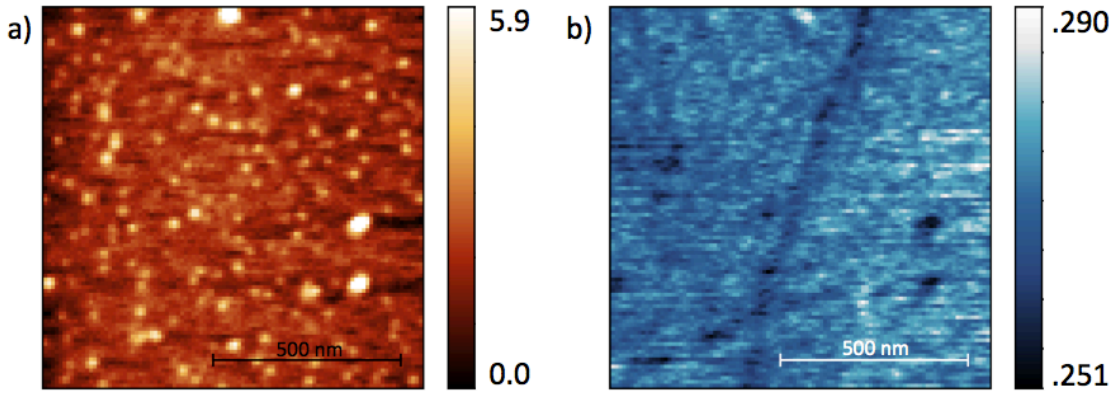

4.2 $MoTe_2$ Raman measurements

As mentioned in section 2.3, Raman spectroscopy has proved a powerful tool in distinguishing different polymorphs of materials. In this phase transition described by Ref. [14], they report a shift from a semiconducting 2H phase with a hexagonal lattice to a conducting 1T' phase with a distorted octahedral geometry. These two distinct lattice shapes should have distinct phonon modes, making Raman ideal for investigating this phase transition.

4.2.1 2H and 1T' characterization

We obtained mechanically exfoliated samples of both the 2H and 1T' phases of $MoTe_2$ mounted on silicon/silicon dioxide substrates. We used our Raman spectroscopy set up to confirm that the Raman spectra from both states agreed with what was reported in Ref. [14]. Low power was imperative for these initial measurements as we had to ensure that in measuring that the phase transition was not induced by these measurements. Our results can be seen in Figure 4.4. In 4.4a, we see our spectra and in Figure 4.4b we have the spectra from Ref. [14]. The spectra for the 2H phases of $MoTe_2$ agreed with each other and agree with what has been reported in the

Figure 4.4: Comparison of Raman measurements on 2H and 1T' states including: a) our measurements; b) Ref. [14] measurements; and c) spectrum from literature [20]

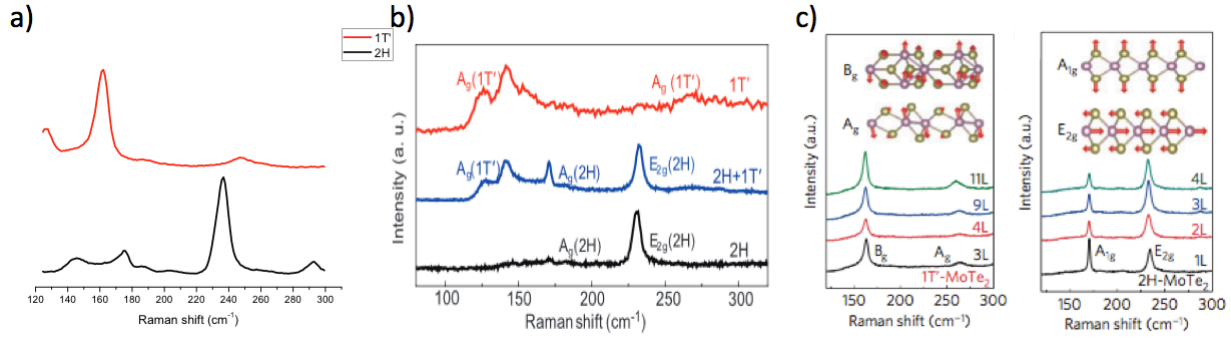

literature[31, 32, 20]. However, the 1T' phases did not agree between our measurements, as seen in the red spectrum in Figure 4.4a as compared to the red spectrum in 4.4b. Comparing to other literature we found Raman spectra from the two phases from [20, 33, 34] that had been measured experimentally with corresponding crystallography measurements and also calculated theoretically. We found that our spectrum did match with what was reported in the literature [20, 33, 34], which all show that the 1T' phase should exhibit a peak around 160 cm^{-1}, with another peak around 250 cm^{-1} that varies with thickness. From this we concluded that we did, in fact, have both the 2H and 1T' phases of $MoTe_2$ and that the reported phase by Ref. [14] was incorrect.

We were also able to detect lower frequency modes than had been previously reported. The spectra in Figure 4.4 only incorporated two fairly high energy modes, the A_g and E_{2g} modes, both which occur above 125 cm^{-1}. Figure 4.5 depicts our thickness dependent measurements of both the 2H and 1T' phases of $MoTe_2$ based upon optical contrast. We can see that our spectra further agree with those found by [20], as they have a similarly reported trend. It appears that the 2H phase sees an increase in the peak intensity at 75 cm^{-1} and has an increase in the E_{2g} peak intensity at 240 cm^{-1} as the structure moves to a bulk form. The 1T' state's B_g peak at 150 cm^{-1} appears to be damped out as the thickness increase. Additionally, the peak near 125 cm^{-1} appears to split into two distinct peaks as the number of layers is decreased.

Figure 4.5: Thickness dependence of Raman results for both the 2H and 1T' phase of $MoTe_2$. We notice that there are several very highly active modes below 125 cm^{-1} that have not been previously reported.

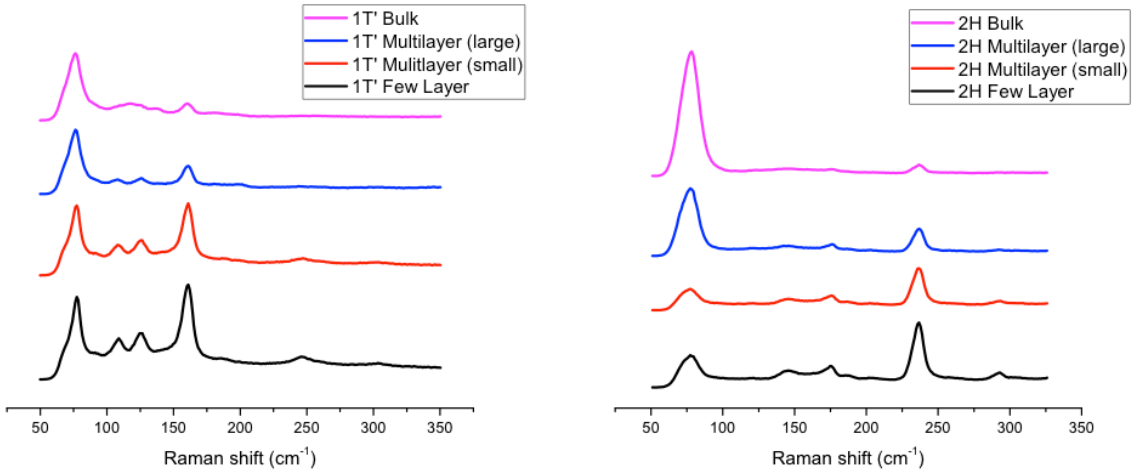

4.2.2 Transitioned states characterization

We focused unattenuated laser light from the 633nm HeNe onto crystals of the 2H phase as well as the 1T' phase and used the developed line scan method in order to create a channel of the transitioned state across each crystal. Observing the crystals after the process we noted that both appeared to have become quite dirty with debris from the ablation, supporting the results from Ref. [14] that the transition ablated the structure to fewer layers. In the case of long exposures to unattenuated laser light, the sample was completely destroyed. Through the optical microscope no distinctive edge was visible in these cases and the Raman spectra from these areas showed only silicon peaks. By reducing the exposure time we could induce the transition without destroying the crystal.

We measured Raman spectra on the ablated regions. Initial spectra had peaks that did not appear in Ref. [14]'s spectrum. The large amount of debris surrounding the sample along with the fact that the transition occurred in atmospheric conditions made Mo and Te oxides a likely candidate for the peaks [35, 36]. After sonicating both 2H and 1T' samples in isopropanol, we remeasured. The spectra from the transitioned states induced on the 2H and 1T' are seen in

Figure 4.6b. The peaks in the 2H spectrum at 200 and 240 cm^-1 we believe are from the debris, corresponding to β-TeO_3 peaks [35]. Numerous cleaning attempts were made but the debris could not be completely eliminated, although the β-TeO_3 peak intensity did decrease from the initial measurements, implying that we were removing this oxide debris from the sample. We also see that the spectra for the transitioned states from both 2H and 1T' state, Figure 4.6b, are identical to that reported in Ref. [14], the red spectrum in Figure 4.6c. The discrepancy in the intenstiy of the peak at 130 cm^-1 in the red spectrum of Figure 4.6c and our in 4.6b is most likely the result of the filter they used cutting off near 125 cm^-1. This means that both the 2H and 1T' phases of these crystal can be transitioned optically to this unknown, transitioned phase.

Figure 4.6: Comparison of Raman spectra reported in: a) our measurements for the unaltered 2H and 1T' states; b) our final, cleaned, and transitioned states of the 2H and 1T' phases; and c) the reported spectrum from Cho *et al*

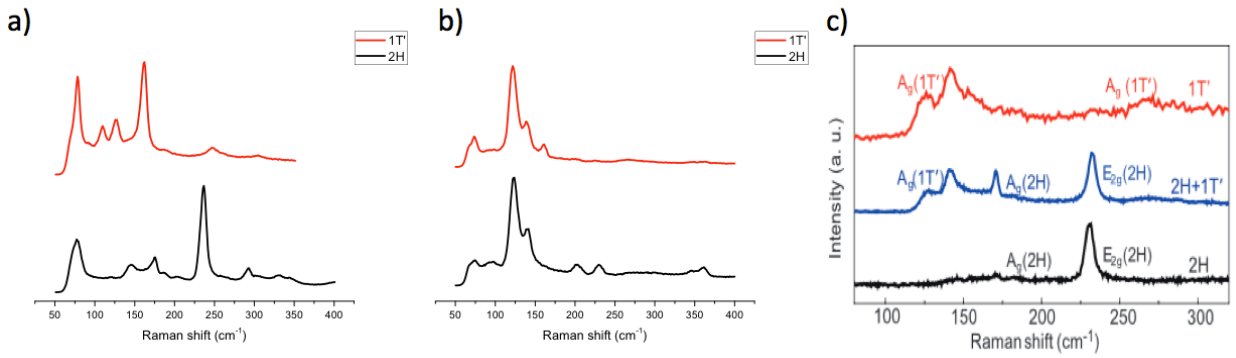

In summary, we found that our spectrum, Figure 4.6a, agree with those reported in the literature [20]. From this, we conclude that the transitioned state reported by Ref. [14] in Figure 4.6c is not the 1T' state. Additionally, we found that this transitioned state can be created from both the 2H and the 1T' phases, as verified by our Raman spectra for the transitioned state, which did in fact agree with the spectra reported in Ref. [14].

A strain induced transition has been reported between the 2H and the transitioned phase [22], labelled as the 1T' but with an identical Raman spectrum to that from the laser transitioned state

which we have confirmed to not be the 1T'. We propose that the underlying mechanism behind this optically induced transition is ultimately a result of heating induced strain. We believe that during the laser ablation process, thermal expansion occurs locally in the focal spot of the laser and resulting in a high strain on the area, transitioning the sample to the transitioned phase.

4.3 MoTe2 near-field measurements

To further investigate the properties of the 2H, 1T', and transitioned phases of these crystals, we conducted s-SNOM to investigate their electronic properties on the nanoscale. Since these materials have not been extensively studied in the near-field before, this work was largely exploratory. By probing with 10.8 μm light, we can assess the conductivity of the sample, allowing for further characterization of the transitioned state.

4.3.1 s-SNOM measurements

Figure 4.7: s-SNOM results on 2H phase. Scan images of the a) topography and b) high resolution topography, c) near-field amplitude and d) high resolution NF amplitude, and e) the near-field phase and f) its zoom.

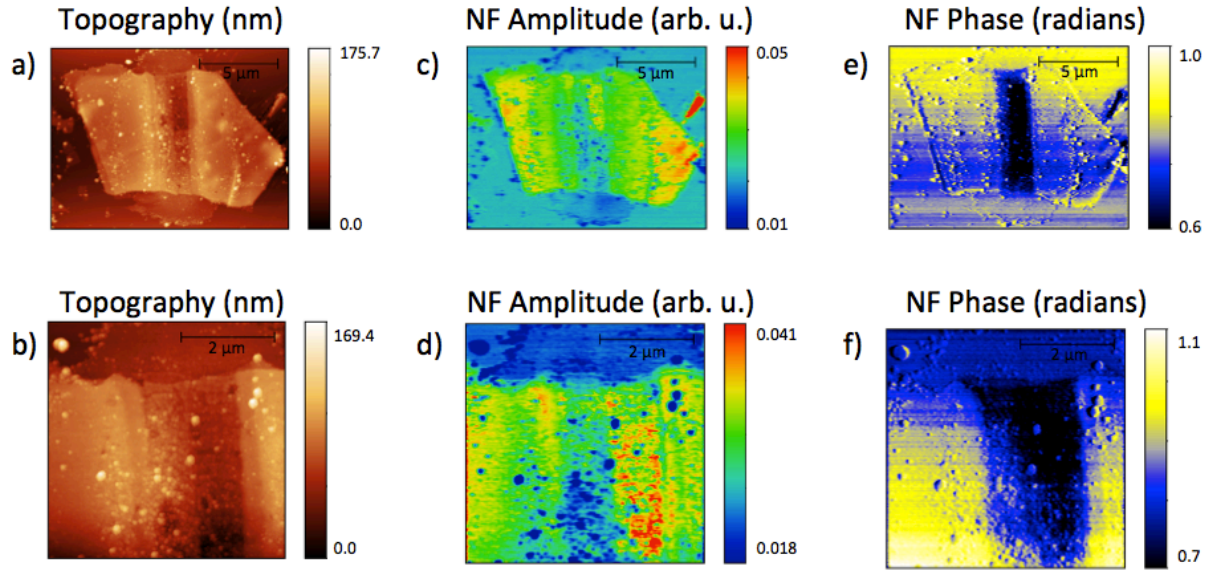

Our first s-SNOM scans were performed on the 2H phase of these crystals. The results can been seen in Figure 4.7. In 4.7a and 4.7b, we see the topography of the entire crystal and a high resolution scan of the transition area. The dark line down the center of the structure is the optically transitioned area. As reported by Ref. [14], we see that the transitioned area has a lower topography than the unaltered areas, proving that the process does cause ablation. The fact that our sample was not ablated to a single layer most likely is the result of a shorter exposure time. The sample is covered with debris, showing up as light spots in the topography. In 4.7c and 4.7d we see the s-SNOM amplitude. Recall, these measurements assess the electronic conductivity. Although the response is heterogenous throughout the crystal and transitioned area, we do not see a strong response in the amplitude in the transitioned area. This is surprising as the transitioned state is theoretically conductive [14]. We do see a slight increase in the area that was focused on slightly longer, which represents the red area in 4.7d. Figures 4.7e and 4.7f are the phase response of the signal. We see a strong phase contrast in the transitioned area, suggesting that there still exist some alteration of electronic behavior in these areas.

Figure 4.8: s-SNOM images of 1T' crystal. The line down the center is the optically transitioned area. We see the a-b) topography of the crystal, c-d) the near-field amplitude, e-f) the near-field phase. Note the change in the amplitude and phase near the top edge of the crystal.

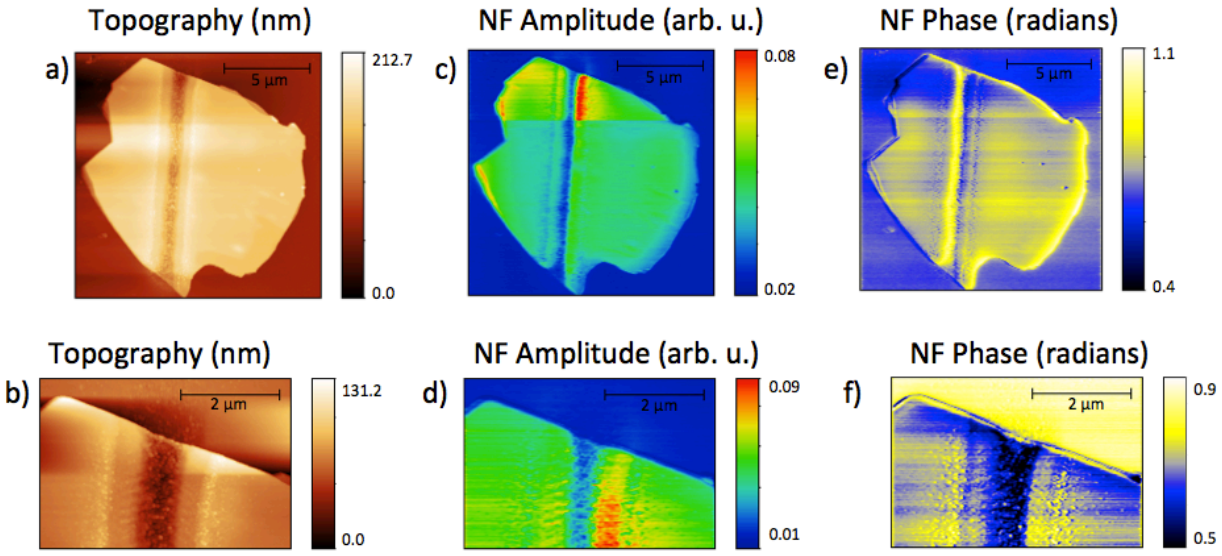

s-SNOM was performed on the 1T' phase with a transitioned channel down the center. Figure 4.8 shows our results. In 4.8a and 4.8b we see the transitioned channel topography is once again lower than the unaltered crystal. This sample is much cleaner than the 2H. 4.8c and 4.8d show the amplitude of the near-field response. The overall amplitude of the response on the 1T' crystal appears greater than that of the 2H, which is consistent with the report that the 1T' is a conducting state and the 2H is semiconducting. Additionally, we notice that in these images that the transitioned area is much less conductive than the 1T' parent crystal. This result is unexpected as Ref. [14] reported that the transitioned state was also conducting, meaning we would expect low contrast between the two phases. A possible explanation for this discrepancy is that the 10.8 μm light used was above the plasma frequency, Equation 2.8, of the transitioned state. As seen in Figure 2.3, a metal is transparent at frequencies above the plasma frequency. This would make the sample invisible to the 10.8 μm light we used and would result in a low response. Figure 4.8e and 4.8f are the phase of the response. The transitioned state appears to, once again, have a drastically different phase response to the 1T' parent. These measurements confirm that this new transitioned state is not the 1T' phase as we see drastic contrast in the optical properties of these two materials.

These scans also revealed something else unexpected. Examining the phase seen in 4.8e and 4.8f, we notice that near the edges there is a sudden increase then an abrupt decrease in the phase at the edge. These affects were reproducible in numerous scans.

Figure 4.9 shows the images from a higher resolution scan on the upper-left edge of the crystal in 4.8. In the topography, Figure 4.9a, we see that the structure is terraced, having several different heights of crystal. In Figure 4.9b we see that the area near the edges have a strong increase in the amplitude of the signal, which is then accompanied by a sudden drop in the phase, Figure 4.9c. Line-cut analysis of these areas, Figure 4.9d-f, reveal that the phase and amplitude change occurs almost immediately after a step in the topography. This highly damped oscillation occurs on the order of 200nm.

To further investigate the possibility of an edge state we wanted to find thinner crystals. We located thinner samples based off optical contrast and repeated our two-phase s-SNOM measure-

Figure 4.9: High resolution s-SNOM images of 1T' crystal's a) topography of the crystal , b) near-field amplitude , and c) near-field phase . We then have the line cut profiles along the line labelled "1" for d) topography e) near field amplitude , and f) phase. Notice the correlation between the edge of the sample in the topography and the rise of the amplitude and phase.

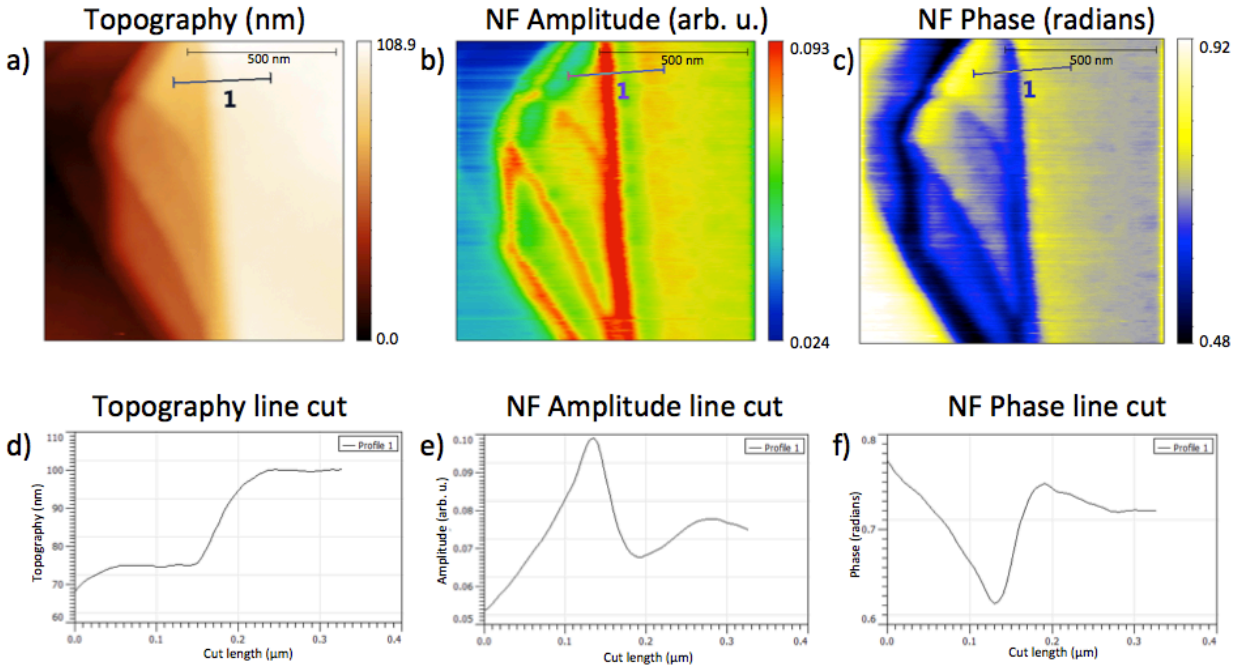

ments on them. Figure 4.10 shows our results. In 4.10a and 4.10b, we have the topography with line cuts and the line cut plots. From these, we can see that the crystal being scanned is roughly 15 nm in height, much smaller than the scanned area in 4.9. 4.10c and 4.10d are the near-field amplitude and the line cut profiles. We see a similar shape in the edge excitation as in Figure 4.9, but here the distance that the effect occurs over is closer to 100nm, half of what was observed previously. The phase measurements for this crystal, 4.10e and 4.10f, reveal a stronger pattern of oscillation than was seen in previous scans, but they are quite noisy.

We then decided to find thin crystal of the 2H phase and see if anything similar would be observed. We located a crystal by optical contrast and performed two-phase homodyne s-SNOM on it. In Figure 4.11 we see the a zoomed image of the edge of this crystal. 4.11a-b, we have the topography and its line cut profile. We observe the crystal is approximately 20 nm in height.

Figure 4.10: s-SNOM images of a thinner 1T' crystal. We see the a) topography of the crystal , c) near-field amplitude, e) near-field phase and their corresponding line cut profiles along the two cuts indicated in each image: b) topography; d) near-field amplitude ; and f) near-field phase.

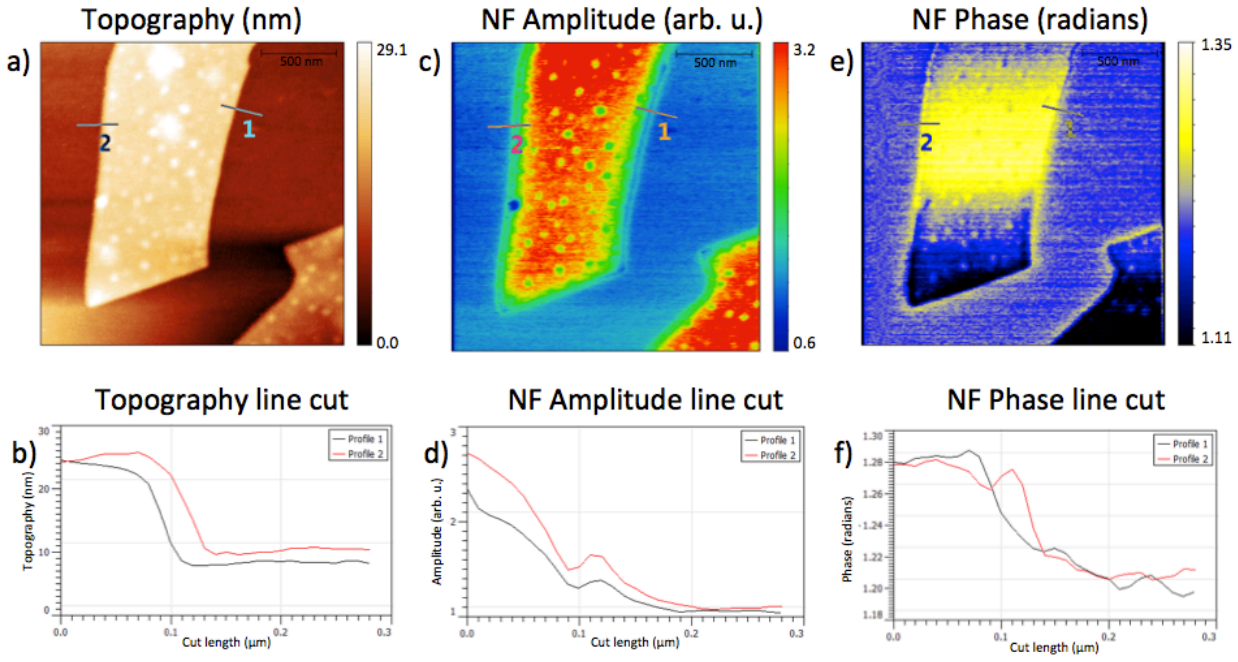

4.11c-d reveal the amplitude and the line cut profile. We see nearly identical behavior to that observed in the 1T' phase. The oscillation is still highly damped and occurs over roughly 100 nm. Figures 4.11e-f are the phase response from this area. Although once again noisy, we see a profile very similar to that observed in Figure 4.9.

Initial hypothesis for these edge states were of a plasmonic nature, much like those seen on graphene in Section 4.1. This result weighed against our initial hypothesis that these edge effects were the results of plasmons, as semiconductors should not support them. However, it is possible that the edges of these crystals are in an alternate state. During the exfoliation process, these samples are ripped from a bulk crystal, which would cause high strain on the edges, which have caused phase transitions in $MoTe_2$. If this were the case, the edges could still support plasmons.

An alternative hypothesis is that this effect is an artifact. As the tip approaches the edge of a sample, the signal would decrease possibly over a distance of the diameter of the tip scanning.

Figure 4.11: s-SNOM images of a thin crystal of the 2H phase where we see the a) topography and b) topography line cut profile, c) near-field signal amplitude and d) line cut profile, and e) near-field phase, and f) line cut profile.

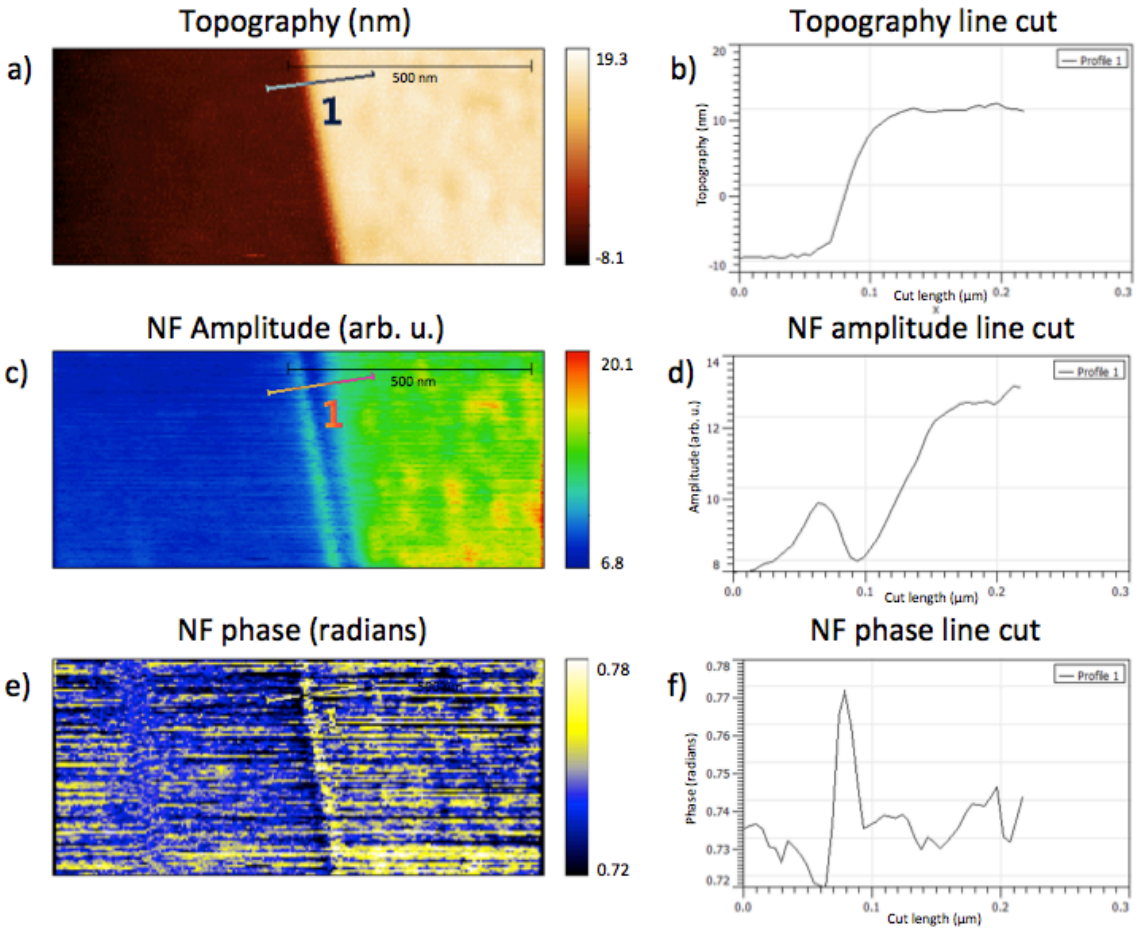

This would be due to the edge of the tip contacting the edge of the sample. Once, however, the tip was more than a diameters distance away, it would then be adjacent to the sample. Recalling figure 2.7a, depicting a tip-image sphere coupling between, we would suppose that in this case the the image sphere would be located in the sample next to the tip, as opposed to below it. This would then give us an increase in signal off of the edge of the sample, which is what we see. This mechanism describes the effect that we are observing. However, if this were the case these edge effects would occur on all samples scanned, which has not been widely reported.

4.3.2 NIST SMM measurement comparison

In addition to the s-SNOM measurements we performed, we measured the electronic properties of the samples at microwave wavelengths. This method is known as impedance near-field imaging or Scanning Microwave Microscopy(SMM). We performed these measurements on 2H crystal as well as the 1T', both of which had the phase transition induced down the center of them. The measurements can be seen in Figure 4.12. Figure 4.12a is a measure of the 2H topography. We see the laser ablated channel down its center. In 4.12b we see the topography of the 1T' phase of the crystal. In this image the transitioned area is from the left to right. Figure 4.12c and 4.12d is the lateral deflection of the tip. As the tip moves across the sample, debris on the sample can deflect it side to side. These measurements reveal the surface texture and can be used to identify debris on the sample. As we see in these images, the transitioned area is prone to debris forming around it. This adds support to the hypothesis that the unidentified peaks in the initial Raman with the peaks were from the Mo and Te oxides. Additionally, this agrees with the transition process described by Ref. [14]. Figure 4.12e is the near-field amplitude of the response from the 2H crystal. These measurements are not phase resolved so we only can observe qualitative differences between the conductivity, not quantitative. We notice that the transitioned area appears to be drastically different in its electronic behavior than the 2H parent phase. In 4.12f, the near-field amplitude of the 1T' and the transitioned state. Here we see a very small contrast between the transitioned area the 1T' parent. From the comparison of these measurements we can infer that the new transitioned state is most likely conducting, as it appear electronically different from the semiconducting 2H but similar to the conducting 1T'.

The contrast in the amplitude of the near-field microwave response we see in these images supports the hypothesis that the 10.8 μm light we probed with s-SNOM was above the plasma frequency of the new state. Microwaves are of a much lower frequency, so we would expect the sample to not completely transmit these longer wavelengths. In these measurements we see that the new state interacts strongly with the microwaves.

Figure 4.12: Scanning microwave microscopy images of the 2H a) topography, b) lateral tip deflection, c) and SMM signal amplitude. Bellow these are the images of a 1T' crystal d) topography, e) lateral tip deflection, and f) SMM signal. Notice the varying contrast between the transitioned area in c) versus in f).

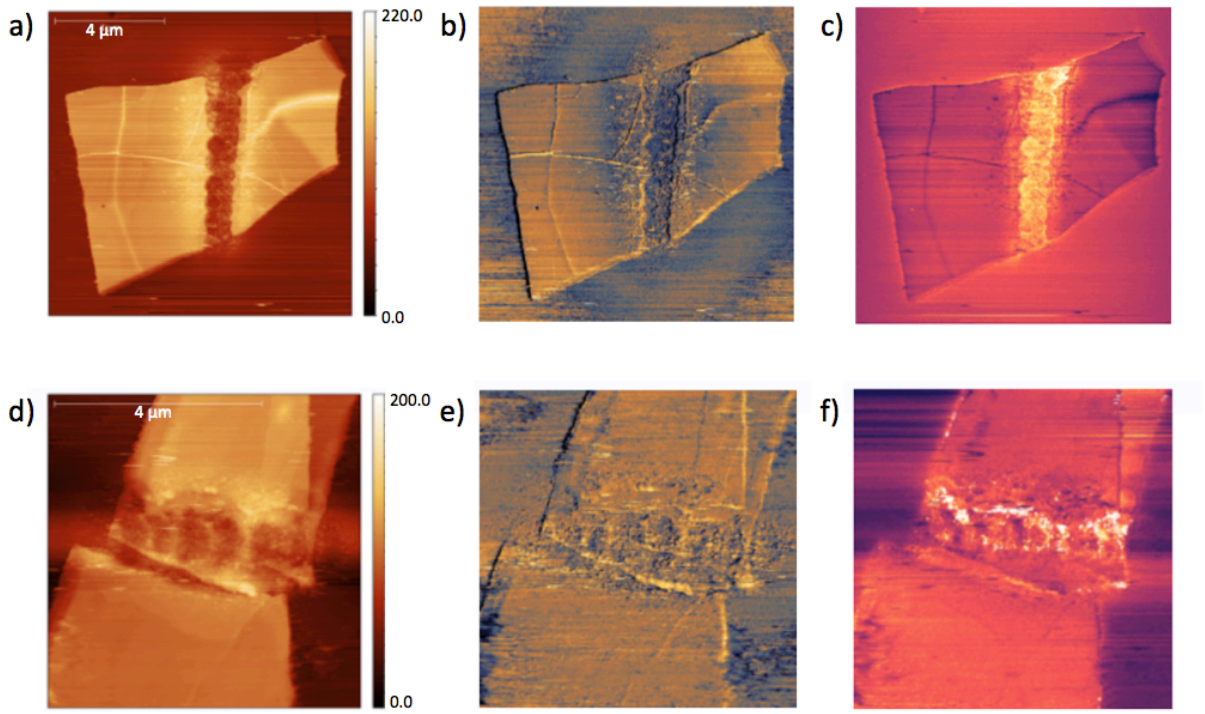

Unfortunately, no SMM scans have yet been taken on the edges of these crystals. We observe a slight increase in the near-field response at the edges of the 2H, but the spatial resolution is not sufficient to determine anything. No effects appear readily visible in the 1T' amplitude.

Chapter 5

Summary, speculation and future work

5.1 Raman lab

Substantial improvements to the Raman spectroscopy set were made. As a result of the optimization process, we experience an increase in signal of nearly an order of magnitude. The resolution of the system has additionally been increased as a part of this process. The translational stage allows for high accuracy in the motion of the stage and the position of the sample. The addition of an enclosure to the system substantially increased the overall stability of the set up and also decreased the amount of background light, giving better accuracy. Overall, these results cumulate in making the system fully ready to perform Raman spectroscopy line scans.

5.2 Graphene

We confirmed the results previously obtained by Gerber *et al* for identifying and measuring surface plasmon polaritons on the edges of graphene. We observed the predicted decaying oscillations of the interfering plasmons. The varying wavelength of the plasmons we observed is a well documented effect that arises from non-uniform charge density through the edges. Additionally, we found this same method to be successful in identifying stacking order defects in bilayer graphene. More measurements were taken on several different samples and we detected other grain boundaries for our collaborators. Future experiments on graphene will be conducted after we receive the samples back from the Pennsylvania State University collaborator. They plan to build contacts for creating devices on these stacking order defects. Possible experiments include flowing current

through these boundaries, allowing us to see how the varying local charge densities affect the overall conductivity of the samples.

5.3 $MoTe_2$

We have observed that the optically induced phase transition reported by Cho *et al* does create a new phase. This structure is not the 1T' state reported by Cho *et al*. We confirmed this with Raman spectroscopy by starting with a sample of the 1T' phase and inducing this transition in it. Our spectrum agreed with that of the transitioned state they reported. We also confirmed with Raman that the 2H phase of $MoTe_2$ can also be transitioned into this new phase. We proposed additionally the idea that this transition is not a result of the illumination, but of the thermal expansion of the local heating leading to strain, which has been shown to create the transitioned phase reported [22]. Moving to the near field, we measured similar responses from the transitioned states created from parent 2H and 1T' crystals, furthering our thought that these states are the same material. The low response and overall decrease in signal that we measured on these samples could be explained by the 10.8μm light we used with being above the plasma frequency of this new state. This would mean that the light we used was transparent to the crystal, resulting in a very low response from the sample. Probing below this frequency would increase the interactions and give better information about this state. The consistence of the Raman spectroscopy results as well as in the s-SNOM measurements allows us to conclude that in the transitioned state is the same regardless of whether the 2H or the 1T' phase was the parent phase. Since there are no similar Raman results for the transitioned state in any of the literature, it is difficult to assess with any certainty as we can't distinctly identify it and thus cannot look into its properties. Further tests to be performed could entail crystallography measurements in order to identify the crystal lattice. Additionally, mass spectrometry of the debris could be particularly insightful as it would help identify the stoichiometry of the debris, giving us insight into the composition of the remain structure.

The edge effects found on both the 2H and 1T' phases require further investigation. Initial

suspicions of highly damped surface plasmons are one possible explanation. The oscillating behavior and the apparent measurement off of the edges supports this idea. The wavelengths observed are short compared to what we observed in graphene, although this could be explained through inhomogeneities in the charge density. The strong damping observed might be a result of the thick samples these effects were observed on. One major problem with the plasmonic nature of this effect is its presence on the 2H phase. Plasmons should only be detectable in metallic materials or doped semiconductors. The sample is not doped, as this would appear in the Raman spectrum and the 2H phase is known to not be conducting. However, it has been reported that a 2H - 1T' transition could occur as a result from strain [22]. During mechanical exfoliation, the process by which these samples were created, the small crystals are stripped from a bulk sample of the crystal by an adhesive. During this process, the samples experience stress and strain. This could result in a 1T' phase existing near the edge of the 2H phase crystals made in this fashion. In this case, the plasmon could in theory propagate off the edges of a 2H crystal. We could possibly identify this with Raman spectroscopy. The discussed Raman line scan procedure would allow us to observe any changes that could occur over the edge. If in scanning over one of these edges we observed any spectral peaks from the 1T' phase, this hypothesis would gain viability. Ultimately, in order to test whether or not this edge effect arises from plasmons, temperature dependent measurements could be performed. $MoTe_2$ has been shown to have a temperature dependent carrier density, so by altering the temperature we would alter the plasmon wavelength. If the edge state wavelength or decay altered with temperature, we would have further support for a plasmonic explanation.

The possibility that this edge effect is an artifact is currently under discussion. The proposed model for explaining this artifact is currently under investigation through mathematical modeling in order to see how the qualitative behavior of such an effect would present itself in various heights of samples with various dielectrics. While possible, the fact that this effect has not presented itself in other materials poses a possible problem for it.

It is also possible that this effect arises from some other known process. The edge states on TMD's have been suspected to show possibly interesting effects [37]. These areas are prone

to different behavior as they lack symmetry along the edge, but any mechanism to produce the observed results would be mere speculation at this point. Further insight could be gained by repeating measurements with different wavelengths of light. Measurements are being planned to perform measurements at the Advanced Light Source at Lawrence Berkeley Laboratories where varying wavelengths are readily available. Additional infrared spectroscopy measurements would be desirable as they would provide additional knowledge about these materials.

Bibliography

[1] Alexander E Mag-isa, Jae-hyun Kim, Hak-joo Lee, and Chung-seog Oh. A systematic exfoliation technique for isolating large and pristine samples of 2D materials. 2D Materials, 2(3):34017, 2015.

[2] Yuan Huang, Eli Sutter, Norman N. Shi, Jiabao Zheng, Tianzhong Yang, Dirk Englund, Hong Jun Gao, and Peter Sutter. Reliable Exfoliation of Large-Area High-Quality Flakes of Graphene and Other Two-Dimensional Materials. ACS Nano, 9(11):10612–10620, 2015.

[3] Xuesong Li, Weiwei Cai, Jinho An, Seyoung Kim, Junghyo Nah, and Dongxing Yang. Large-Area Synthesis of High-Quality and Uniform Graphene Films on Copper Foils. Science, 2009:1–12, 2009.

[4] Qing Hua Wang, Kourosh Kalantar-Zadeh, Andras Kis, Jonathan N Coleman, and Michael S Strano. Electronics and optoelectronics of two-dimensional transition metal dichalcogenides. Nature Nanotechnology, 7(11):699–712, 2012.

[5] Britton W H Baugher, Hugh O H Churchill, Yafang Yang, and Pablo Jarillo-Herrero. Optoelectronic devices based on electrically tunable p-n diodes in a monolayer dichalcogenide. Nature nanotechnology, 9(4):262–7, 2014.

[6] Claudia Ruppert, Ozgur Burak Aslan, and Tony F. Heinz. Optical properties and band gap of single- and few-layer MoTe2 crystals. Nano Letters, 14(11):6231–6236, 2014.

[7] Mahito Yamamoto, Sheng Tsung Wang, Meiyan Ni, Yen Fu Lin, Song Lin Li, Shinya Aikawa, Wen Bin Jian, Keiji Ueno, Katsunori Wakabayashi, and Kazuhito Tsukagoshi. Strong enhancement of Raman scattering from a bulk-inactive vibrational mode in few-layer MoTe2. ACS Nano, 8(4):3895–3903, 2014.

[8] Long Ju, Zhiwen Shi, Nityan Nair, Yinchuan Lv, Chenhao Jin, Jairo Velasco, Claudia Ojeda-Aristizabal, Hans A. Bechtel, Michael C. Martin, Alex Zettl, James Analytis, and Feng Wang. Topological valley transport at bilayer graphene domain walls. Nature, 520(7549):650–655, 2015.

[9] Chun Hung Lui, Zhiqiang Li, Kin Fai Mak, Emmanuele Cappelluti, and Tony F. Heinz. Observation of an electrically tunable band gap in trilayer graphene. Nature Physics, 7(12):10, 2011.

[10] Lukas Novotny. The History of Near Field Optics. Cambridge Press, 2006.

[11] Joanna M Atkin, Samuel Berweger, Andrew C Jones, and Markus B Raschke. Nano-optical imaging and spectroscopy of order, phases, and domains in complex solids. Advances in Physics, 61(6):745–842, 2012.

[12] A. Bogner, P. H. Jouneau, G. Thollet, D. Basset, and C. Gauthier. A history of scanning electron microscopy developments: Towards "wet-STEM" imaging. Micron, 38(4):390–401, 2007.

[13] Lukas Novotny. Chapter 5 The history of near-field optics. Progress in Optics, 50:137–184, 2008.

[14] Suyeon Cho, Sera Kim, Jung Ho Kim, Jiong Zhao, Jinbong Seok, Dong Hoon Keum, Jaeyoon Baik, Duk-hyun Choe, K J Chang, Kazu Suenaga, Sung Wng Kim, Young Hee Lee, and Heejun Yang. Phase patterning for ohmic homojunction contacts in MoTe2. Science, 349(6248):625–628, 2015.

[15] Sergey Gaponenko. Introduction to Nanophtonics. Cambridge University Press, 2010.

[16] Emilie J Siochi. Graphene in the sky and beyond. Nature Nanotechnology, 9(10):745–747, 2014.

[17] Oleg V Yazyev and Steven G Louie. Electronic transport in polycrystalline graphene. Nature materials, 9(10):806–809, 2010.

[18] Gianluca Fiori, Francesco Bonaccorso, Giuseppe Iannaccone, Tomás Palacios, Daniel Neumaier, Alan Seabaugh, Sanjay K. Banerjee, and Luigi Colombo. Electronics based on two-dimensional materials. Nature Nanotechnology, 9(10):768–779, 2014.

[19] K S Novoselov, A K Geim, S V Morozov, D Jiang, Y Zhang, S V Dubonos, I V Grigorieva, and A A Firsov. Electric field effect in atomically thin carbon films. Science (80-.)., 306:666–668, 2004.

[20] Dong Hoon Keum, Suyeon Cho, Jung Ho Kim, Duk-Hyun Choe, Ha-Jun Sung, Min Kan, Haeyong Kang, Jae-Yeol Hwang, Sung Wng Kim, Heejun Yang, K. J. Chang, and Young Hee Lee. Bandgap opening in few-layered monoclinic MoTe2. Nature Physics, 11(6):482–486, 2015.

[21] a K Geim and I V Grigorieva. Van der Waals heterostructures. Nature, 499(7459):419–25, 2013.

[22] Seunghyun Song. Room temperature semiconductor–metal transition of mote2 thin films engineered by strain. Nano Letters, 2016.

[23] Kin Mak, Changgu Lee, James Hone, Jie Shan, and Tony Heinz. Atomically Thin MoS_{2}: A New Direct-Gap Semiconductor. Physical Review Letters, 105(13):136805, 2010.

[24] Mark Fox. Optical Properties of Solids. Oxford Press, 2010.

[25] Oliver Benson. Assembly of hybrid photonic architectures from nanophotonic constituents. Nature, 480(7376):193–199, 2011.

[26] Justin A. Gerber, Samuel Berweger, Brian T. O'Callahan, and Markus B. Raschke. Phase-resolved surface plasmon interferometry of graphene. Physical Review Letters, 113(5):1–5, 2014.

[27] Vasily Kravtsov. Plasmonic nanofocused four-wave mixing for femtosecond near-field imaging. Nature nanotechnology, 2016.

[28] Zhe Fei, Gregory O. Andreev, Wenzhong Bao, Lingfeng M. Zhang, Alexander S. McLeod, Chen Wang, Margaret K. Stewart, Zeng Zhao, Gerardo Dominguez, Mark Thiemens, Michael M. Fogler, Michael J. Tauber, Antonio H. Castro-Neto, Chun Ning Lau, Fritz Keilmann, and Dimitri N. Basov. Infrared nanoscopy of dirac plasmons at the graphene-SiO2 interface. Nano Letters, 11(11):4701–4705, 2011.

[29] Meisam Rahmani. The effect of bilayer graphene nanoribbon geometry on schottky-barrier diode performance. Journal of Nanomaterials, 2013.

[30] Joshua D. Caldwell. Van der waals heterostructures: Mid-ir photonics. Nature materials, 2015.

[31] Nazila Haratipour and Steven J. Koester. Multi-layer MoTe2 p-channel MOSFETs with high drive current. Device Research Conference - Conference Digest, DRC, (612):171–172, 2014.

[32] Ignacio Gutiérrez Lezama, Ashish Arora, Alberto Ubaldini, Céline Barreteau, Enrico Giannini, Marek Potemski, and Alberto F. Morpurgo. Indirect-to-Direct Band Gap Crossover in Few-Layer MoTe¡inf¿2¡/inf¿. Nano Letters, 15(4):2336–2342, 2015.

[33] Jin Cheol Park, Seok Joon Yun, Hyun Kim, Ji Hoon Park, Sang Hoon Chae, Sung Jin An, Jeong Gyun Kim, Soo Min Kim, Ki Kangk Kim, and Young Hee Lee. Phase-Engineered Synthesis of Centimeter-Scale 1T???- and 2H-Molybdenum Ditelluride Thin Films. ACS Nano, 9(6):6548–6554, 2015.

[34] Yanpeng Qi, Pavel G Naumov, Mazhar N Ali, Catherine R Rajamathi, Walter Schnelle, Oleg Barkalov, Michael Hanfland, Shu-Chun Wu, Chandra Shekhar, Yan Sun, Vicky Sü, Marcus Schmidt, Ulrich Schwarz, Eckhard Pippel, Peter Werner, Reinald Hillebrand, Tobias Förster, Erik Kampert, Stuart Parkin, R J Cava, Claudia Felser, Binghai Yan, and Sergey A Medvedev. ARTICLE Superconductivity in Weyl semimetal candidate MoTe 2. Nature Communications, 7:1–48, 2016.

[35] J. C. Champarnaud-Mesjard, S. Blanchandin, P. Thomas, A. Mirgorodsky, T. Merle-M??jean, and B. Frit. Crystal structure, Raman spectrum and lattice dynamics of a new metastable form of tellurium dioxide: ??-TeO2. Journal of Physics and Chemistry of Solids, 61(9):1499–1507, 2000.

[36] M. Dieterle and G. Mestl. Raman spectroscopy of molybdenum oxides. Physical Chemistry Chemical Physics, 4(5):822–826, 2002.

[37] Xiaobo Yin, Ziliang Ye, Daniel a Chenet, Yu Ye, Kevin O'Brien, James C Hone, and Xiang Zhang. Edge nonlinear optics on a MoS atomic monolayer. Science (New York, N.Y.), 344(6183):488–90, 2014.

[38] G. Binnig and C. F. Quate. Atomic Force Microscope. Physical Review Letters, 56(9):930–933, 1986.

[39] Yao Li, Karel-Alexander N. Duerloo, Kerry Wauson, and Evan J. Reed. Structural Semiconductor-to-Semimetal Phase Transition in Two-Dimensional Materials Induced by Electrostatic Gating. Nature Communications, pages 1–8, 2016.

[40] Min Kan, Hong Gi Nam, Young Hee Lee, and Qiang Sun. Phase stability and Raman vibration of the molybdenum ditelluride (MoTe2) monolayer. Physical chemistry chemical physics : PCCP, 17(22):14866–71, 2015.

[41] Yao Zhou and Evan J. Reed. Structural Phase Stability Control of Monolayer MoTe ¡sub¿2¡/sub¿ with Adsorbed Atoms and Molecules. The Journal of Physical Chemistry C, 119(37):21674–21680, 2015.

[42] Jiong Yang, Tieyu L??, Ye Win Myint, Jiajie Pei, Daniel Macdonald, Jin Cheng Zheng, and Yuerui Lu. Robust Excitons and Trions in Monolayer MoTe¡inf¿2¡/inf¿. ACS Nano, 9(6):6603–6609, 2015.

[43] Tigran V. Shahbazyan and Mark I. Stockman. Plasmonics: Theory and Applications. 2013.

[44] Manish Chhowalla, Hyeon Suk Shin, Goki Eda, Lain-Jong Li, Kian Ping Loh, and Hua Zhang. The chemistry of two-dimensional layered transition metal dichalcogenide nanosheets. Nature chemistry, 5(4):263–75, 2013.

[45] Bernhard Knoll and Fritz Keilmann. Enhanced dielectric contrast in scattering-type scanning near-field optical microscopy. Optics Communications, 182(4):321–328, 2000.

[46] Karel-alexander N Duerloo, Yao Li, and Evan J Reed. Structural phase transitions in two-dimensional. Nature Communications, 5(May):1–9, 2014.